# Using geomatics techniques to reveal mineralization alteration zones in Southwestern Sinia. A study in mineral geomorphology.

**Dr. Heba Allah Mohamed Mokhtar**
Ph.D. of Geomorphology and GIS
Geography and GIS Department, Alexandria University, Egypt
h.mokhtar@alexu.edu.eg

## Abstract:

This study employs geomatics techniques to study minerals according to their geological origins and landforms features. Thus, it is one of the mineral geomorphological studies using the advanced methods. Especially nowadays, it is indispensable to use satellite visuals for detecting minerals before starting the mining process which is considered to be an initial excavation process. This study aims to use the ASTER image to survey and discriminate the mineralization zones in Southern Sinai in general and the Southwestern Coast of Sinai in specific. Studying the geological setting to understand the origin and formation conditions of mineralization. Discussing the topographic evidences and the mineral's effects on the geomorphological and landforms features which help to identify the minerals in the field. Mapping the minerals-bearing rocks and areas currently exploited to identify the promising areas. Besides, studying the road network in the region that facilitates the mining process.

It has been studied eight mineral alteration zones. Oxides minerals as iron oxide and manganese oxide, Carbonate, Clay as propylitic, phyllic and argillic, Sulfide, Silica, and silicate minerals. Many of these include hydrothermal zones containing economic minerals such as gold and copper. Therefore, mineral maps have been produced and displayed samples showing landforms and associated minerals. With clarification of the most important mineral sites in the region and explain the reasons for mineral concentration in some areas more than others. The results revealed that the East Ras Malaab area and Wadi Feiran are the richest and the most diverse mineralization areas in the Southern Sinai.

**Keywords:** Geomatics techniques - Mineralization zones – ASTER - Geomorphological features – promising areas.

# 1. Introduction:

Developing the earth's resources, especially the minerals has become a focus of most countries because of its high economic returns. Minerals exist in several forms such as residual deposits, placer deposits, in veins and dykes, filling fractures and joints, or as an alteration zone which is the most valuable which this is the field of study. Therefore, minerals will be studied from its relation to the geological and geomorphological settings. Using ASTER "Advanced Spaceborne Thermal Emission and Reflection Radiometer" is an effective image satellite in discriminating and classifying rocks and minerals. Because of containing three subsystems VNIR, SWIR, and TIR that consist of 14 bands. So, analyzing the ASTER image helped to achieve the aims of the study. Depending on the geomatics techniques represented in the programs and the methods applied, as will be discussed later in detail. This is an advanced technique providing the efforts, cost, and time-consuming of mineral exploration.

This research point has been applied to the region of Southern Sinai due to its richness in mineral wealth. Which has been exploited since ancient times by the Pharaohs, but it is full of minerals that have not been exploited until our time. Therefore, it needs more studies to determine its importance and discover its locations. The proposed study area occupies 31.780 $km^2$ and is located between the Suez and Aqaba Gulfs, at 27˚43'23.3"to 29˚57'46"N and 32˚36'24"to 34˚55'10.58"E. Where the rock formations and geological structures vary widely. This reflected in the availability of mineral wealth in the region. Its geologic evolution was passed by five major geological events, the Precambrian, Paleozoic, Mesozoic, Tertiary, and Quaternary ages. In addition to being affected by the major structural lineaments such as faults, fractures, dykes, shear zones, and folds hinges and their densities. It is an indicator for accurately identifying areas of hydrothermal alteration zones. Geomorphological features help to recognize the alteration zones from three aspects, some landforms of structural origin evidence of minerals aggregation and its lithology determine its appearance in the field, geomorphological history helps in knowing the conditions of minerals formation and gathering, and some minerals have direct effects on the landform of the study area. Therefore, this research will focus on studying the different landforms and their evolution through their

relationship with minerals in the region. Here, light is shed on one of the important branches of applied geomorphology, which is mineral geomorphology.

The study aims to map the mineralogic zones in Southern Sinai and determine the most and the least minerals-containing areas. For achieving economic development and encouraging local and foreign investors to invest their capital in the mineral exploration field. With the evaluation of the road network which serves the area.

- **Literature review:**

***Shendi et al., (2008):*** traced the magnetic and gravity data in South Sinai to detect the promising mineral areas. While ***Madani and Emam., (2011):*** studied the basement rocks at El Hudi area in Southeastern Desert, Egypt. They are focused on the SWIR ASTER to discriminate the rocks which cover the area for designing the lithological map. Which will be a clue to identify the minerals derived from the metasedimentary rocks on which they are based. ***Yousefi et al., (2018):*** discriminated the hydrothermal alteration zones related to porphyry Cu deposits such as sericite, kaolinite, epidote, and quartz which hosted by granitoids in Kerman province, Iran. They accomplished the research by using Principal Component Analysis (PCA) and Minimum Noise Fraction (MNF) methods. ***Salehi (2019):*** discussed the ASTER possibilities to detect mineral alterations in Greenland depending on four methods, band ratio, band combination, PCA, and MNF. ***Oha et al., (2021):*** employed PCA and MNF to demonstrate the ferric, ferrous oxides, sulphide, and silica alterations related to Zn, Pb, and Ba minerals in Nigeria. ***Ali Bik et al., (2022):*** using three types of satellite images, ASTER, Landsat 8, and Sentinel 2 to distinguish the lithology of Wadi Abu-Qada and Wadi Wata and the exposed Oligo-Miocene basalt and the minerals.

## 2. Objective:

The article discusses six objectives:

1. Study of hydrothermal alteration zones by using different images processing techniques.
2. Studying the geological setting of the mineral alteration zones. To know the circumstances of its origin.

3. Discussing the geomorphological features of minerals in the field. Which helps specialists in identifying minerals during fieldwork.
4. Overlaying and comparing the results reached and the currently exploited areas. To identify the promising mineralization areas.
5. Studying the current road network to determine whether the promising areas have available facilities or not.
6. Conducting a case study on the most important mineralization area in the basement and sedimentary rocks.

## 3. Material and methods:

### 3.1. ASTER image data:

ASTER image is a very effective image that helps to explore and determine sites of minerals. ASTER has three subsystems, visible and near infrared VNIR, shortwave SWIR, and thermal infrared TIR. And, orthorectified digital elevation model (dem). *ASTER VNIR* including four bands, its resolution is 15 meters. In fact, has three bands. Because band 4 has the same wavelength as band 3, the first enhancing the visual interpretation angle by 27.5˚. *ASTER SWIR* including six bands, its resolution of 30 meters. *ASTER TIR* consisting of five bands, its resolution of 90 meters. **Table (1)**

**Table (1): Subsystem and Spectral bands of ASTER image**

| Subsystem | Spectral bands | Wavelength range (µm) | Spatial resolution |
|---|---|---|---|
| VNIR | 1 | 0.52-0.6 | 15 |
| | 2 | 0.63-0.69 | |
| | 3N | 0.76-0.86 | |
| | 3NB | 0.76-0.86 | |
| SWIR | 4 | 1.600-1.700 | 30 |
| | 5 | 2.145-2.185 | |
| | 6 | 2.185-2.225 | |
| | 7 | 2.235-2.285 | |
| | 8 | 2.295-2.36 | |
| | 9 | 2.36-2.43 | |
| TIR | 10 | 8.125-8.475 | 90 |
| | 11 | 8.475-8.825 | |
| | 12 | 8.925-9.275 | |
| | 13 | 10.25-10.95 | |
| | 14 | 10.95-11.65 | |

**Source:**https://lpdaac.usgs.gov/data/get-started-data/collection-overview/missions/aster-overview/

## 3.2. Pre-processing of ASTER data:

ASTER satellite image (AST14DOM) of the study area, **downloaded** from https://asterweb.jpl.nasa.gov. ASTER VNIR and ASTER TIR bands were satisfying, but Aster SWIR bands were excluded. Because since April 2008 not been useable which showed saturation values and severed striping. So, Aster SWIR data was collected in the period 2001-2007. Which consists of 21 scenes. **Fig (1)**

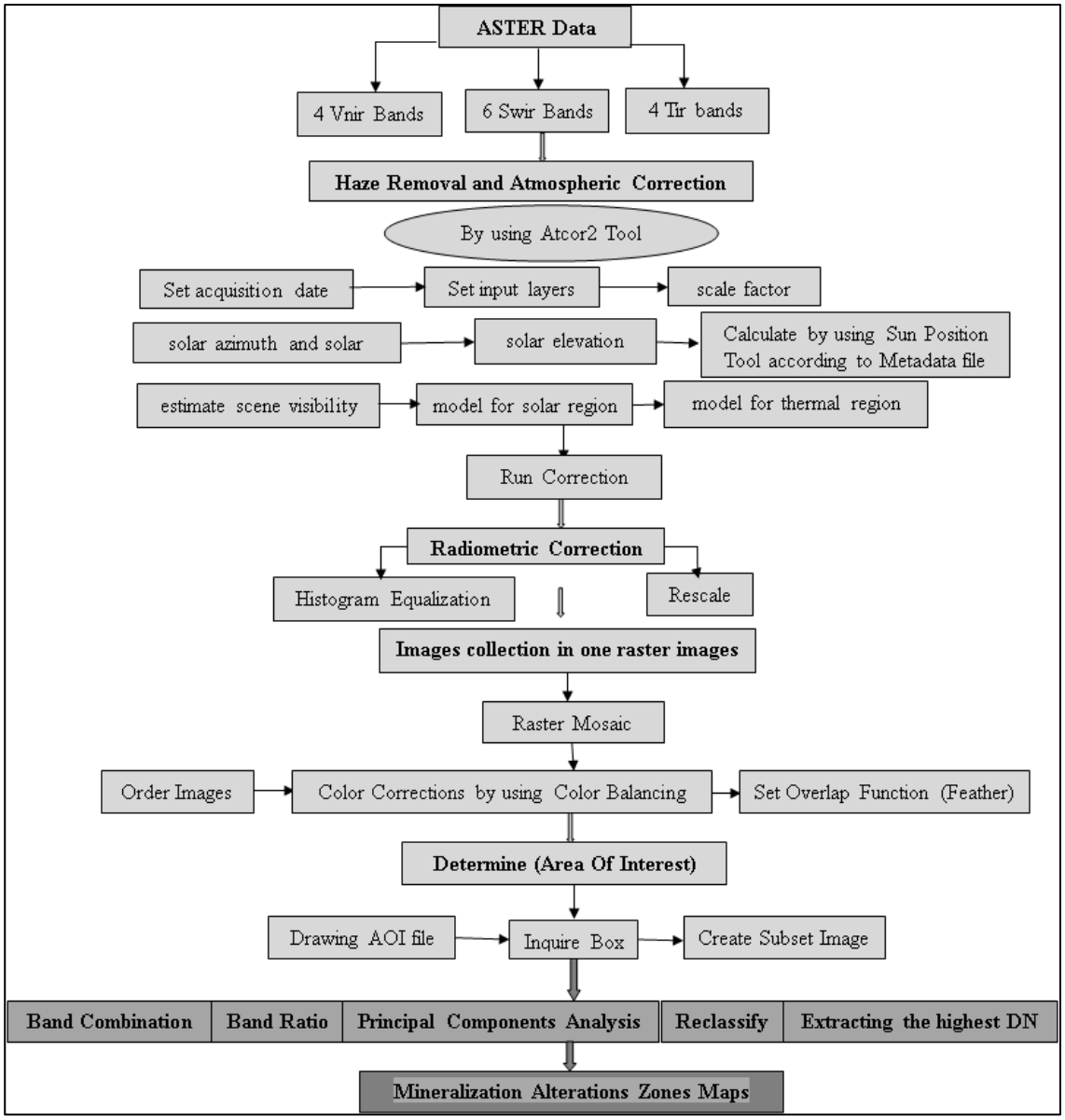


**Figure (1): Methodology of processing and analysis ASTER data**

**Layer stack tool**, to collect and combine the multiple bands files that have the same resolution in a single file. Results in the output of three files, VNIR, SWIR, and TIR. After that, resample the three files' bands to combine them in one file which including the 14 bands with the same pixel size of 90m. To be easier and faster to deal with and perform various operations. **Haze removal and atmospheric correction** were applied by using the Atcor2 Tool. It's an extension tool that is added to the toolbox of ERDAS Imagine14 program. That module helps to remove the haze of image as vapor, moisture, dust, and smokes in the atmosphere. Which negatively affects the ability of visual interpretation. This can be done by providing it with data according to the metadata file. As the date of taking the image, solar zenith and solar elevation. This process is applied to each image.

**A radiometric correction** was applied by using two tools. Firstly, the histogram equalization method is an image processing of contrast adjustment. By redistributing the digital values of the most frequent intensity values to highlight the low-contrast image. Secondly, the rescale method is applied after the previous method to stretch the values of the image between the minimum value of 0 and the maximum value of 255. **Collect multiple corrected raster** images in one raster by using the Mosaic tool. Order images by bring forward or back, color correction by color balancing and set overlap feather. **Determine the area of interest (AOI).** To subset the study area and its boundaries. Therefore, the product raster will be higher resolution and faster in processing. Therefore, **Figure (2)** shows the final product after processing the ASTER data by using band combination.

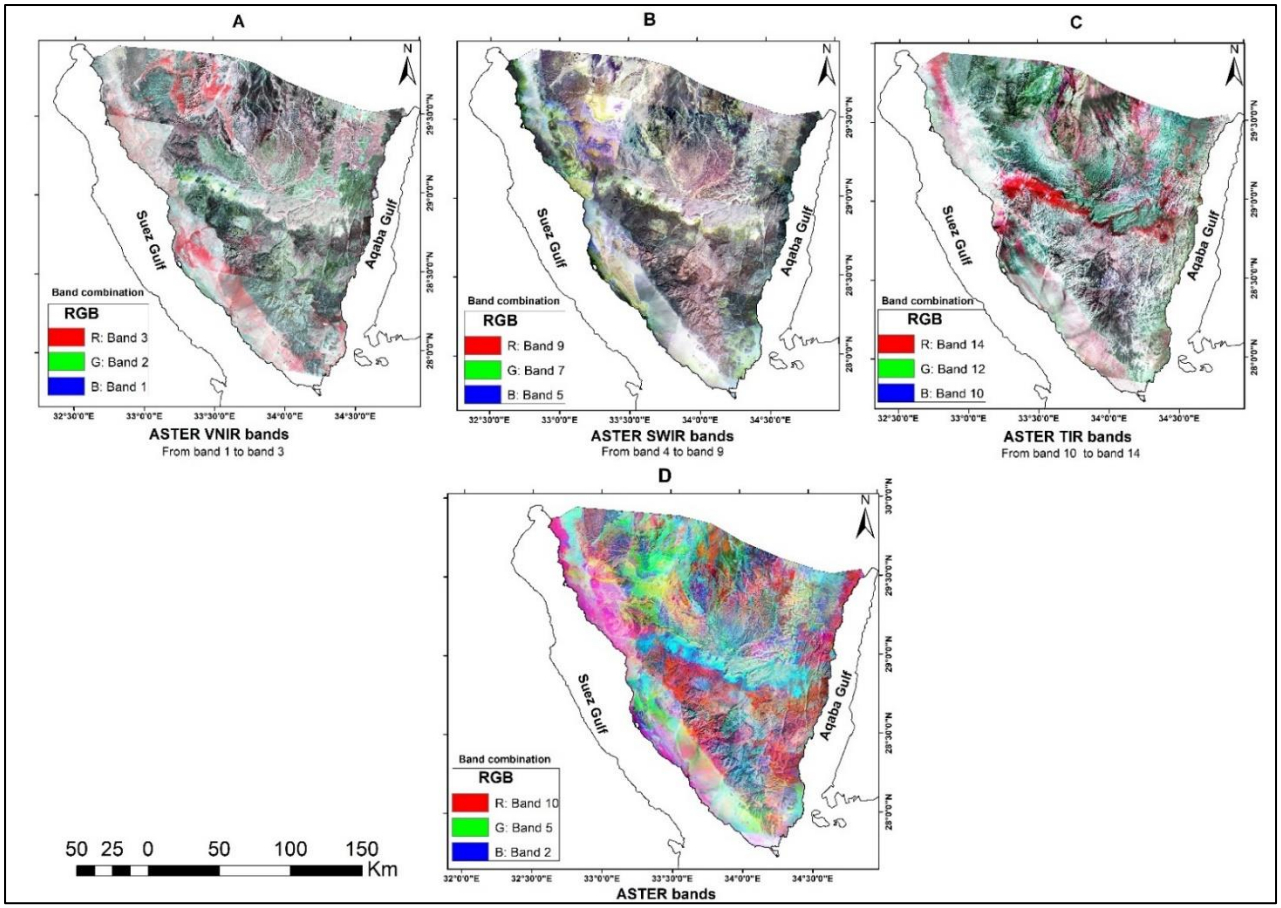


**Figure (2): ASTER data "VNIR, SWIR, and TIR" after processing**

**Source:** processing the Aster data and applying the band combination method to each subsystem separately, and entirely.

## 3.3. Analysis of ASTER data:

### 3.3.1. Band ratio:

It has been applied the band ratio method to analyze the ASTER image in the mineral's exploration field. Accordingly, it was designed 15 minerals maps of southern Sinai. Also, each mineral map has been classified from the most to the least mineral-containing areas. The band ratios applied in this study are mentioned in **Table (2)**.

**Table (2): The applied and the excluded band ratio in the study area**

| Major group minerals | Feature | Mineral index | | Economic & industrial minerals | Bearing rocks |
|---|---|---|---|---|---|
| | | Band ratio | References | | |
| Clay | Chlorite / epidote / amphibole (Propylitic) (Mg-OH) | (B6+B9)/(B7+B8) | Khunsa & Rehman (2017) | Porphyry copper, quartz, pyrite, orogenic gold, epithermal gold, chromite deposits, massive sulfides, iron and shales | Volcanic rocks |
| | | (B7+B9)/B8 | Salem, et al., (2018) | | |
| | | B5/B8 | | | |
| | Muscovite / Smectite / Sericite / Illite (Phyllic) (AL-OH) | (B5+B7)/B6 | Khunsa & Rehman (2017) | | Calc-alkaline and preamble rocks |
| | | B5/B6 | Salem, et al., 2018 | | |
| | Kaolinite/ Alunite/ Montmorillonite (Argillic) (AL-OH) | (B4+B6)/B5 | Kaliknowsski & Oliver (2008) | | Igneous rocks and weathered sandstone |
| | | B4/B5 | | | |
| | Kaolinite | (B4/B5)*(B8/B6) | Pour & Hashim., (2011) | Clay minerals | Weathered rocks contain mica and silica |
| | Muscovite | B7/B6 | Salehi, et al., (2019) | | |
| | Phengite | B5/B6 | Khunsa & Rehman (2017) | | |
| | Montmorillonite | (B4+B6)/B7 | Khunsa & Rehman (2017) | bentonite | Glass volcanic and in sedimentary rocks that consists of mud beds |
| | Alunite | (B7/B5)*(B7/B8) | Pour & Hashim., (2011) | Gold, silver | Volcanic rocks |
| | Alunite / kaolinite / pyrophyllite | (B4+B6)/B5 | Kaliknowsski & Oliver (2008) | Economic minerals | Low degree of the metamorphism rocks |

| | | | | | |
|---|---|---|---|---|---|
| Carbonate B13/B14 (B5+B6+B9)/ (B7+B8) | Calcite | (B7+B9)/B8 | Khunsa & Rehman (2017) | Calcium, Magnesium, iron, Manganese | Limestone & ultramafic |
| | | (B6/B8)*(B9/B8) | Pour & Hashim., (2011) | copper malachite and azurite | |
| | | B8/B7 | Beirami & Tangestani (2020) | | |
| | Dolomite | (B6+B8)/B7 | Khunsa & Rehman (2017) | Carbonate minerals | Dolostone |
| | | (B5+B9)/B7)/((B 6+B9)/B8) | Beirami & Tangestani (2020) | | |
| | Magnesite | (B6+B8)/(B7+B9) | Khunsa & Rehman (2017) | | Calcite & basement |
| Iron oxide | Ferrous ($F^{3+}$) | B2/B1 | Sengupta, et al., (2018) | Limonite – Hematite – Jarosite – Goethite. | Weathering of ferrous sulfide and carbonate &Volcanic acid rocks |
| | | B3/B1 | Singh & Mandla., (2020) | | |
| | Ferric ($F^{2+}$) | (B5/B3)+(B1/B2) | Kaliknowsski & Oliver (2008) | Ferrous minerals | Sandstone, metamorphosis rocks & mafic dykes |
| | Siderite | B5/B4 | Oha, et ai., (2021) | | |
| | Laterite | B4/B5 | Kaliknowsski & Oliver (2008) | | |
| | Gossan | B4/B2 | | | |
| | euhedral apatite mineralization | B4/B1 | Malainine, et al., (2021) | | |
| | Ferrous Silicates | B5/B4 | Sengupta, et al., (2018) | | |
| Manganese Oxide | Magnesia | B5/B6 | Kaliknowsski & Oliver (2004) | | Sandstone contains iron beds and igneous rocks |
| Silica and Silicate | Quartz | [B11/(B10+B12)] *(B13/B12) | Aboelkhair, et al., (2020) | Quartz, K-feldspar, pyrite. Sand | Granite especially the younger type and sandstone |
| | Siliceous rocks abundance | (B11*B11)/(B10* B12) | Pour & Hashim., (2011) | | |
| | | B2/B9 | Oha, et ai., (2021) | | |
| | | B13/B10 | | | |
| | | B14/B12 | | | |
| | | B13/B14 | | | |
| | | B13/B12 | | | |
| Sulfide | Sphalerite, Pyrite & Pyrrhotite | (B1+B3)/B2 | Oha, et ai., (2021) | Copper, Zink, Lead, Gold, Silver, Nickel, Cobalt, | Widespread in all rocks but with minor quantities |
| | Pyrite | B3/B4 | | | |

| | | | | | |
|---|---|---|---|---|---|
| | Sulfides in unoxidized environments | B1/B4 | | Cadmium, Molybdenum. | especially Volcanic & gneiss rocks |
| Mafic | Olivine, pyroxene, amphibole | B12/B13 | Pour & Hashim., (2011) | Ferromagnesian minerals | Rocks contain calcium and plagioclase feldspar. Igneous rocks rich in magnesium and iron. |
| Hydroxyl bearing minerals | | (B7/ B6)*(B4/B6) | Pour & Hashim., (2011) | Economic minerals | Propylitic, Phyllic &Argillic |

***Blue fonts refer to the indexes applied in the study.**

### 3.3.2. Band ratio combination:

It's another method applied in the study area. Which helped to explore many minerals and discriminate the lithology of area. There are 7 maps have been designed by following this method. The bands' combinations applied are mentioned in **Table (3)**.

**Table (3): The applied band combination in the study area**

| Major group mineral | Features | Band combination | References |
|---|---|---|---|
| Manganese Oxide | magnesia | (RGB) (B1+B3)/B2, (B5+B7)/B6, (B3+B5)/B4 | Rajendran & Nasir., (2013) |
| Silicate | Siliceous rocks abundance | RGB B13/B10, B13/B12, B13/B14 | Oha, et ai., (2021) |
| | | RGB B13/B10, B14/B12, B13/B14 | |
| Hydrothermal Alternation Zone | Argillic, Phyllic, Propylitic | RGB B4/B6,B5/B6,B5/B8 | Rani, et al., (2020) |
| | | PCA2, PCA4, PCA6 | Applied the PCA to the study area |
| Argillic alteration | Economic minerals | B5/B6, B7/B6, B7/B5 | Alkashghari, et al., (2020) |
| Sulfide alteration | | R:12, G:5, B:3 | Alkashghari, et al., (2020) |
| Iron Oxides | | PCA2, PCA2, PCA2 | Applied the PCA to the study area |
| Carbonate | | PCA3, PCA3, PCA3 | |

### 3.3.3. Principal Components Analysis (PCA):

This method aims to enhance the results to be more accurate and specific. Following two directions. First, to determine the highest component of each studied mineral PCA. To reach the richest and poorest mineral regions. Second, by using the Hopkins University

Spectral Library (JPL) https://speclib.jpl.nasa.gov/documents/jpl_desc to recognize the spectral fingerprints of the minerals in ASTER image. Determination of reflection and absorption bands at the level of many metals forming the alteration zones. The method helps identify the most diverse alteration with minerals. This is evident in 13 maps in the study.

### 3.4. Post-analysis ASTER:

Using PCI Geomatica Banff 2020 program to extract the structural lineaments automatically from the ASTER image. Depending on the Algorithm Librarian from lineaments extraction. And using the Line Density tool in ArcGIS 10.8 program to calculate the density of faults by km per $km^2$. And using the Pan Sharpening tool in ArcGIS to identify the dykes in an easy visual way and then extract them manually.

Linking the produced layers to geological features to stand out the formation conditions of minerals. And matching them with geomorphological phenomena to know their impacts on landscape and how to identify each alteration mineralization zone by an easier way.

Pure pixels of mineral ores were identified in all raster data produced according to the histogram of each mineral. By applying the "Reclassify tool" in ArcGIS to divide each raster layer into two classes, one of them represented the areas of high variance mineral. Then overlay the minerals' layers on AOI. Which helped to distinguish areas containing certain minerals and not others.

The extracted results were overlayed on the currently used mines and quarries. To identify the unexploited and promising areas in the future, which helps to estimate the geological reserve. And was overlayed on the road network layer. To determine the areas served by good network and the suffering areas which need to establish infrastructure.

## 4. Geological setting:

### 4.1. Lithological units:

***The Precambrian rocks;*** include six rock suites. ***Metamorphic rocks;*** are two suits. *genesis rocks* which including paragenesis (quartz biotite genesis), orthogenesis (hornblende biotite genesis), with mylonite, migmatite amphibolite, calc-silicate, and metabasite dykes **(Abu El-Enen,et al., 2013).** *Metavolcanic rocks* are divided into five sub-groups, metamorphosed volcanogenic sediments, metamorphosed volcanic

schist, metamorphosed intermediate volcanics, metamorphosed acid volcanics, and metamorphosed pyroclastic volcaniclastic. Exposed in Sedri, Sahu, Feiran, Solaf, south of Taba, northwest of Nuweibaa, Qubilaa, Ghorabi, Um Adawi, Kid basin, Sharm El-Shiekh. ***Ultra-mafic rocks;*** named *Mélange Dahab – Attar*; which is including coarse to medium-grained metagabbro, metadiorite, chrysotile bearing serpentinite dunnite mélange, albitite, and quartz-diorite. In Feiran basin as Wadi El-Akhdar and Solaf, Wadi El-Bidaa, Saal – Zaghra, Tuwibaa, wadi Kid, and Qabr Bniaa. ***Calc-alkaline rocks;*** including two rocks suites. *Ferani suite (GI);* including quartz-diorite, granodiorite, tonalite, quartz monzodiorite. Dokhan volcanics as feldspar and quartz porphyries rhyodacite **(El-Masry, et al., 1992).** *Rahba suite (GII);* including olivine hornblende gabbro, monzogranite, syenogranite and monzonite. Widespread in the study area, as many parts of Feiran, Watir, Mahash, Dahab, Kid basins, Wadi Rim, Taba, Sharm El-Shiekh, and other areas. ***Alkaline rocks;*** named *Kathrine suite (GIII).* Because of the abundance of its outcrops in that area. In addition, Taba, South of Wadi Mahash, and parts of Abu Durba Mountain. Including alkaline granite, syenite, quartz-syenite, and granophyre dykes. ***(Hermina, et al., 1989)***

***The Paleozoic rocks****; Cambrian rocks*; are sandstone rocks in some areas interbedded with ferruginous beds at Wadi Araba and manganese ore that occur near Um Bugma. *Carboniferous rocks*; consist of sandstone with intercalations of carbonaceous clay at Abu Durba. Dolomite and dolomite limestone rich in carboniferous fossils occur in Um Bugma, which contains manganese and iron solution and manganese pockets.

***The Mesozoic rocks****; Triassic rocks*; are alternate beds sandstone and red shale. Occurs near Abu Zneima and Abu Rudies. *Jurassic rocks*; are yellowish-white well bedded sandstone. *Cretaceous rocks*; lower Cretaceous is sandstone intercalated with mudstone and siltstone. Kaolinitic gaps are common, and form the south of El'Tih plateau escarpment. Upper Cretaceous is limestone rocks with marl and clay intercalations. It extends from the east of Suez Gulf to the west of Aqaba Gulf, as a large basin form located at south of El'Tih and Ajma Plateaus. Noticing limestone partly dolomitic in Wadi Wata in Raha plateau. Furthermore, limestone enclosing phosphatic rock interbeds in the southern parts of Ajma.

***The Tertiary rocks****; are* divided into five rock groups. *Paleocene rock*, represented in Esna Formation, it's green shale and marl enclosing carbonate intercalations. Occurs in Wadi Sedri, Raha, and northwest Nazazat mountains. *Eocene rock*, is limestone interbeds with marl where widespread in El'Tih, Ajma plateaus and Abu Zneima. *Oligocene rock*, is a basal conglomerate topped with red siltstone and limestone. Characterized by the presence of basalt flows at the top. And, occurs in central Sinai at the coast of Suez Gulf. *Miocene rock*, is alternate beds of sandstone, marl, and limestone. In some parts, anhydrite, gypsum, and dolomite appear. With some volcanic intrusions as dykes, sills, and lava of olivine, basalt, and dolerite. Appears from Ras Masalh to the north of Ras Malaab. *Pliocene rock*, is divided according to genesis into three formations. Estuaric deposits as in the north of Al Qa'a plain, marine rocks as in Ras Mohamed, and alluvial deposits as in the lower part of Wadi Feiran and some estuaries of wadis that flow into Aqaba Gulf. **(Hermina, et al., 1989)**

***The Quaternary rocks****; Pleistocene,* has continental facies as alluvial Hamada deposits, fanglomerate deposits, and Watir Formation. And, coastal facies as coral reefs. *Holocene*, has continental facies as sand dunes, playa, and wadi deposits. And, Coastal facies as sabkha deposits. **Fig (3)**

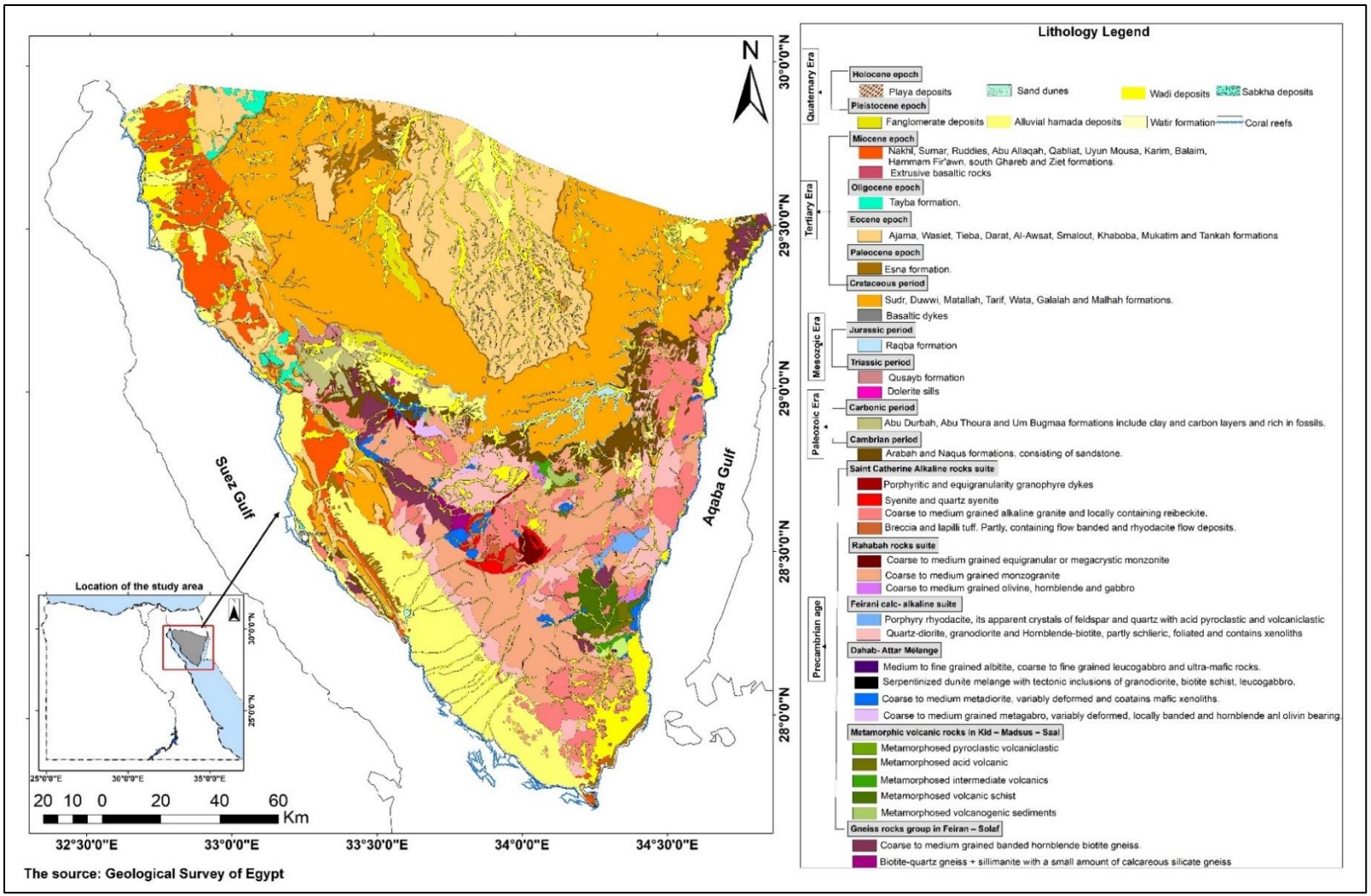


**Figure (3): The lithology of the South of Sinai**

**Source:** Three sheets of Egypt's geological maps scale 1: 250.000

## 4.2. Geological structures:

*Faults and fractures;* There are many directions of faults. The most relevant, are the NW-SE and NE-SW directions **(Lyberis, 1988)**. While the least in N-S and E-W directions. The faults density increases in the northwest of region in Miocene and Cretaceous rocks, in Nuwiebaa - Taba, middle of Feiran Basin, west and middle of Dahab Basin, Kid, and Sharm El-Shiekh area. **Fig (4)**

*Shear zone;* It can be ductile in sedimentary and metamorphic rocks or brittle in metamorphic and igneous rocks. Or the two kinds as in metamorphic rocks. Here, the most important areas are in Saint Kathrine province and Wadi El-Shiekh in Feiran, where the intersection points of faults represent the hydrothermal alteration zones. **(Mohamed, 2013)**

*Folds;* Help the geologist to know the hydrothermal bearing mineral deposits movement. Especially, along to the hinge zone which is a geological weakness line. In metamorphic rocks, it's mesoscopic folds in the rock texture. As, in Wadi Feiran and Solaf, Kid Basin, Saal - Zakhraa in Dahab Basin, and south of Taba. Occur in sedimentary rocks as major structural units. **(Fowler et al., 2015, Kusky., 2002, El-Bialy & Ali., 2013)**

*Dykes;* Are varied between mafic as basalt and dolerite, intermediate as andesite, and felsic as dacite, rhyolite, granite, and granophyre. Dykes has many directions NE-SW, NW-SE, and N-S. **(El-Sayed., 2006)** The density of dykes increasing in Feiran Basin, Agramia area in Dahab Basin, Nuwiebaa – Dahab area, Kid Basin, and Sharm El-Sheikh. Especially, in the northwest of basement rocks, which occur as swarms. **Fig (5)**

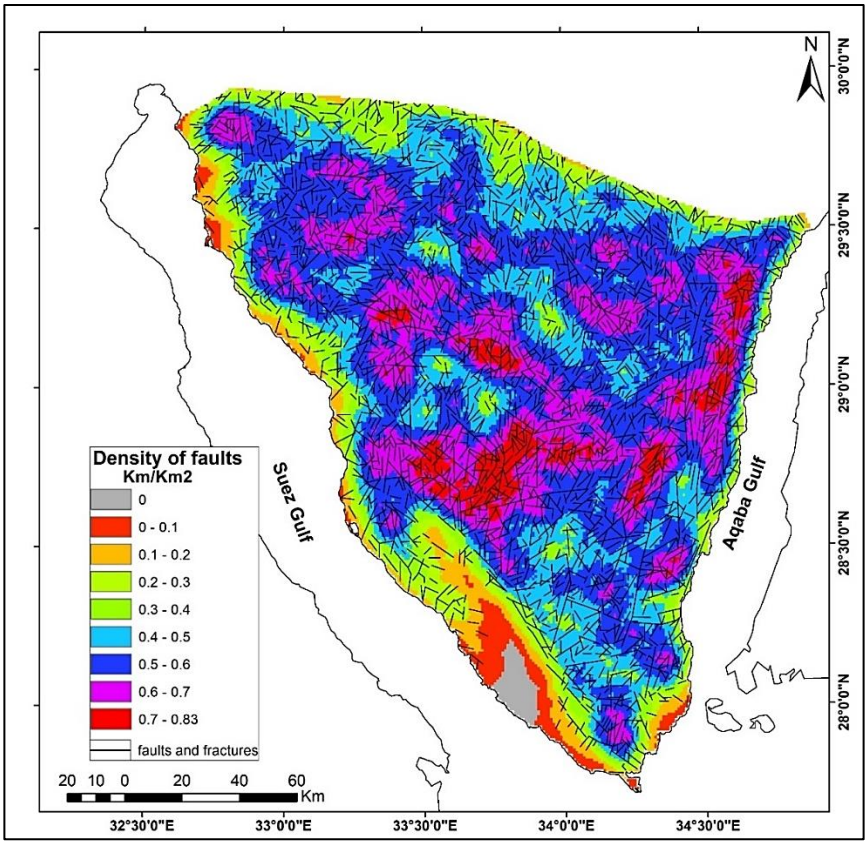


**Figure (4): Density of faults and fractures in the South of Sinai**

**Source:** extracting the structural lineaments by using PCI Geomatica Banff program and applying the Line Density tool by using arc map.

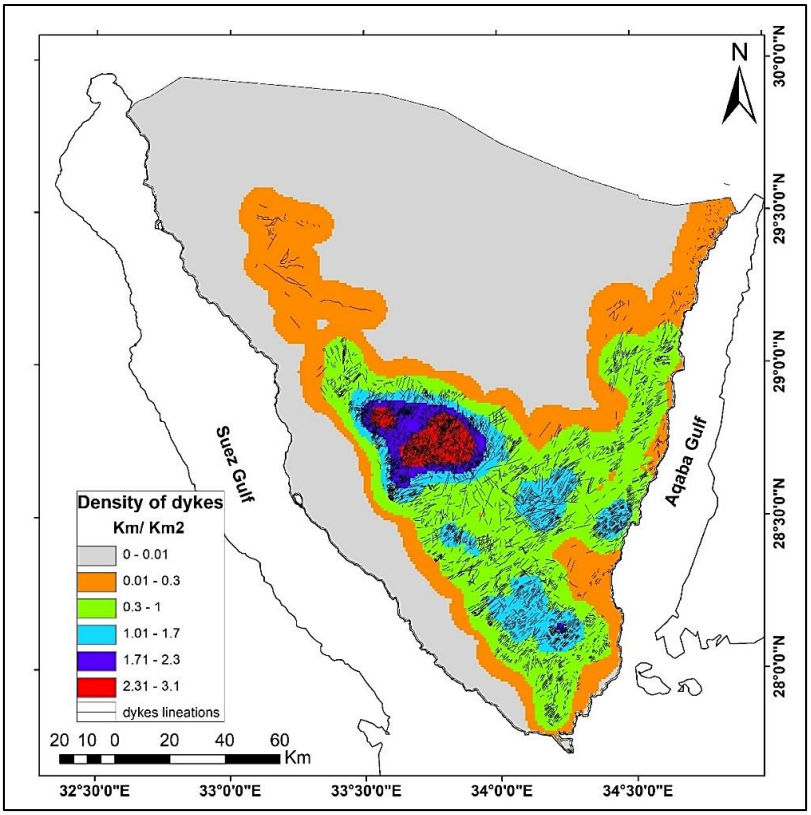


**Figure (5): Density of dykes in the South of Sinai**
**Source:** using the Pan Sharpening tool and Line Density tool in arc map.

## 5. Geomorphological setting:

The region has a variety of landforms. Divided into three major types; mountains, plateaus, and coastal plains. Its maximum elevation is up to 2635m. In general, it is noted that the fault ridge appears in the form of a wall on the eastern coast of the region, and in many cases, it does not leave a beach in front of it, while the opposite of this appears on the western side of the region, where the fault ridge appears severely receding, leaving a wide coastal plain in front of except a few parts.

The southern basement mountainous triangle has a head at the south at the Red Sea and a base in the north at 29˚57'46"N. Interspersed with wadis, playa, and fanglomerate deposits. Faults' effects led to the raising of the valleys' path levels. So, hanging wadis occur at the east and south of the basement rocks. Also, gorges are widespread in the region due to the effects of faults and dykes in the igneous rocks. There are many

batholitic plutons of granites that dissected by structural lineaments. In addition to, some basement terrain such as domes, clitters, and roof pandent. This triangle is bounded from the north by the sedimentary plateaus of El'Tih and Ajma. It overlooks the surrounding area through a topographic escarpment. Some landforms related to the limestone rock appear on their surfaces such as gorges, blind wadies, sinkholes, and lapies "Khrafish" due to the karstic processes in the cretaceous formations. Hogbacks scattered on the west side, and, hills, mesas, and buttes on both sides of sedimentary rocks. **Fig (6)**

The eastern and western margins of the region are bordered by coastal plains. Containing deltas of valleys that pour into the Aqaba and Suez Gulfs. Sabkhas, lagoons, and sand barriers appear along to the coasts, especially the Suez Gulf coast. **Figure (7) & Figure (8)** show longitudinal and cross sections of the area.

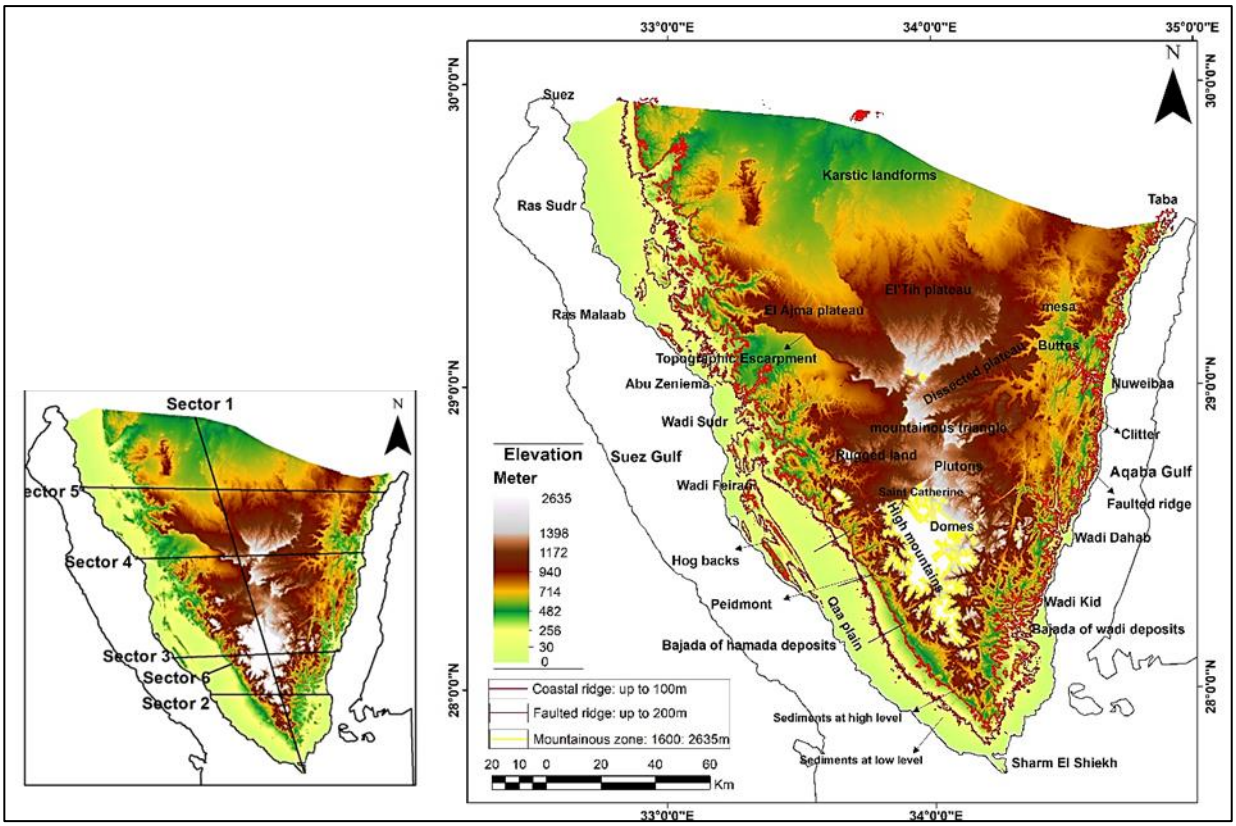


**Figure (6):** Digital Elevation Model (DEM) of the study area. The left map shows the geographic locations of the topographic cross sections.

**Source:** classifying the elevations of DEM and interpreting the landforms**.**

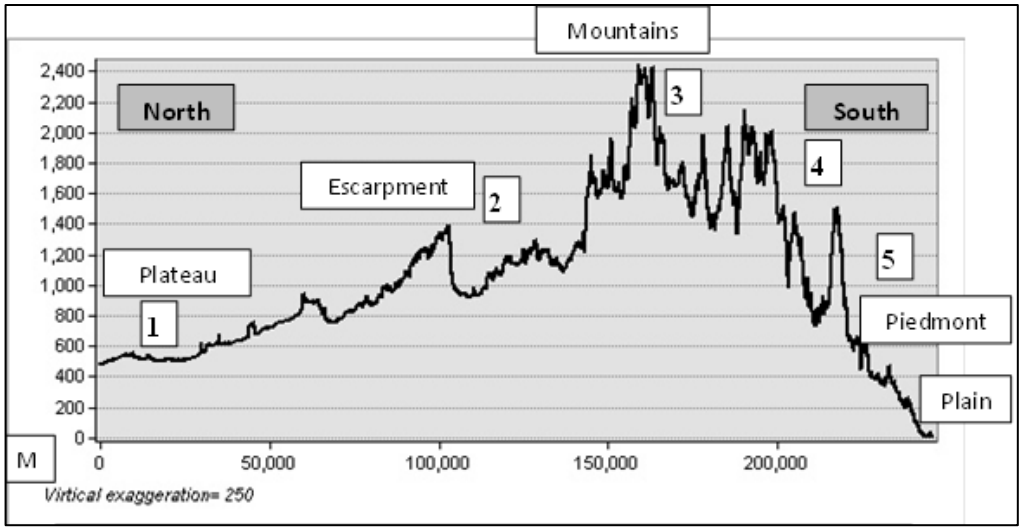


**Figure (7):** The longitudinal profile of the study profile of the study area extends from north to south

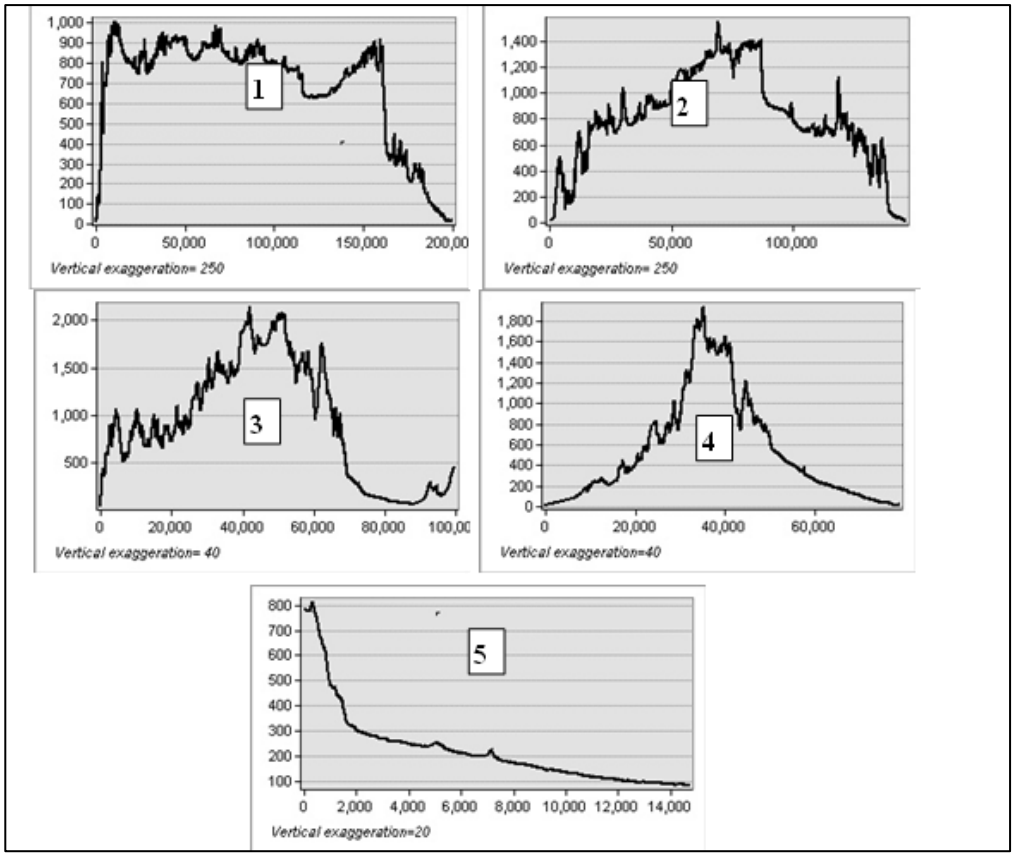


**Figure (8):** the cross profile of the study area, 1&2 the plateau landform, sector 3 & 4 the mountainous landform, and sector 5 the piedmont coastal plain.

# 6. Results and discussion:

## 6.1. Minerals groups:

### 6.1.1. Iron Oxide minerals:

The ASTER band ratio B2/B1 is more effective in the ferric oxide alteration zones than B3/B1 **(Singh & Mandla., 2020)**. The first band ratio is sensitive in the detection of the rocks bearing minerals. While the other band ratio in the deposits bearing minerals. At the same time, it was used the band ratio (B5/B3) + (B1/B2) in ferrous oxide alteration and B5/B4 in ferrous silicate **(Sengupta. et al., 2018)**. Furthermore, using the JPL helped to identify the reflectance bands 2, 3, and 5 and the absorption bands 1 and 4 of the iron minerals in general. Then the principal components analysis was applied which revealed that PCA3 is the highest value in bands 2 and 1. Also, the PCA was applied individually to the three alterations, which revealed PCA2 is the highest value in each of the three alterations. The band combination method was applied "R (ferric oxide), G (ferrous oxide), B (ferrous silicate)". **Table (4 to7) & Fig (9) & Fig (10)**

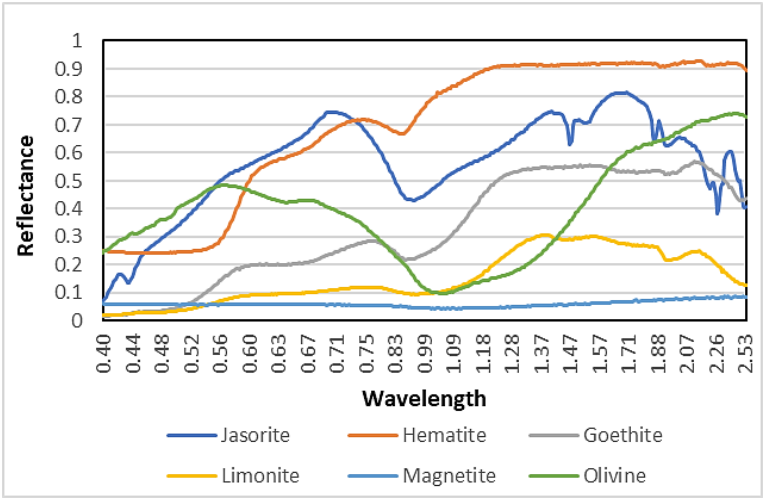


**Figure (9): Spectral signature of Iron Oxide minerals from JPL library**

**Source:** download data from https://speclib.jpl.nasa.gov/documents/jpl_desc. And using the EXCEL application to represent the wavelength, and the spectral reflectance, and design the graph.

***Table (4): Eigenvalues and Eigenvectors of PCA's Ferric Oxides**

| PCA | Band 1 | Band 2 |
|---|---|---|
| 1 | 0.70805 | 0.70616 |
| 2 | 0.70616 | 0.70805- |

***Table (5): Eigenvalues and Eigenvectors of PCA's Ferrous Oxides**

| PCA | Band 1 | Band 2 | Band 3 | Band 5 |
|---|---|---|---|---|
| 1 | 0.50822 | -0.35934 | 0.23249 | -0.74735 |
| 2 | 0.50785 | -0.40034 | 0.38597 | 0.65791 |
| 3 | 0.51377 | -0.01795 | -0.85271 | 0.09274 |
| 4 | 0.46887 | 0.84278 | 0.26431 | -0.00415 |

***Table (6): Eigenvalues and Eigenvectors of PCA's Ferrous Silicates**

| PCA | Band 4 | Band 5 |
|---|---|---|
| 1 | 0.72763 | 0.68597 |
| 2 | 0.68597 | -0.72763 |

***Table (7): Eigenvalues and Eigenvectors of PCA's Iron Oxides**

| PCA | [1]2 ↑ | 1 ↓ | 3 ↑ | 4 ↓ | 5 ↑ | Average |
|---|---|---|---|---|---|---|
| **1** | 0.45013 | 0.42118 | 0.24715 | -0.0308 | -0.74696 | 0.379244 |
| **2** | 0.44942 | 0.45264 | 0.4003 | 0.02774 | 0.65736 | 0.397492 |
| **3** | 0.45239 | -0.55076 | 0.11552 | -0.69126 | 0.02878 | 0.367742 |
| **4** | 0.45753 | 0.17995 | -0.866 | 0.01507 | 0.09001 | 0.321712 |
| **5** | 0.42594 | -0.53103 | 0.12397 | 0.72126 | -0.03148 | 0.366736 |

Reflectance bands ↑ | Absorption bands ↓ | The highest correlation of PCA

***Source:** applying the principal components method and analysis the output to extract the highest correlation coefficient regardless of the negative signal.

[1] **Note:** The studying bands were arranged alternately between reflection and absorption in order to reach the highest correlation coefficient between bands.

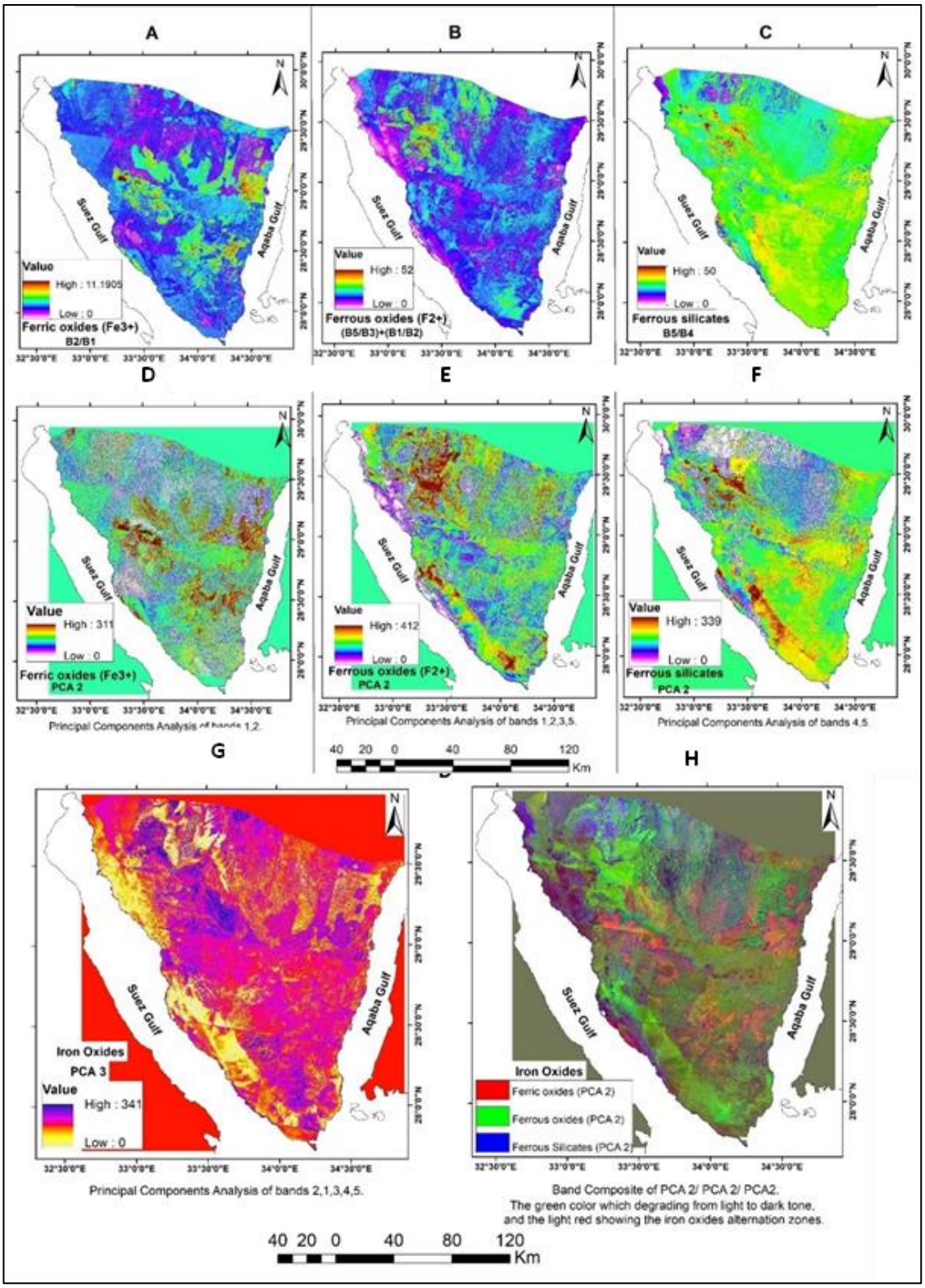


**Figure (10): Iron oxides alternation zones in the South of Sinai**

***Geological setting,*** occurred in the sedimentary Cambrian, Triassic, Miocene, and Eocene rocks. In low, medium, and high-grade metamorphosed rocks such as chlorite-biotite schist zones, epidote-amphibolite, and sillimanite respectively. The early crystallization stage of ultramafic rocks especially metagabbro which located above the alkaline rocks. When plagioclase is replaced by alkali feldspar such as hematite. **(Anovitz., 2021)**

***Geomorphological features,*** **t**he oxidation process of minerals is accompanied by a mineralization slump or oxidation subsidence, especially in limestone. Resulting from the contraction of minerals-bearing rocks causing rock-fall at the foot of slopes and the appearance of steep fissures and fractions that separate the rich rocks from the surrounding areas **(Pirajno., 1992)**. Knowing the landform evolution of topography and hydrogeology is very important for understanding the oxidation process, as it affects the recurrent weathering process that the area is exposed to. These include chemical weathering due to precipitation, which causes dissolution, and mechanical weathering due to stress, which forms solutions. Which leads to the formation of oxidation alterations according to the rock formation that helps to form it. Such as, in granite spheroidal weathering and the presence of pore-size distributions. **(Anovitz., 2021)**

Occurred as *banded iron formation* in the alternating layers of the sedimentary rocks. And in the medium dissected folded mountains, domes, and roof pandent in the basement rocks. The high-grade bands are present in the hydrothermal alteration zones in which the density of faults ranges between 1:0.5 to 1: 0.8 km/km$^2$. *Residual iron deposits* are due to the concentration and accumulation of iron material over a long time by disintegration, fragmentation, and decomposition of rocks (weathering). *Placer deposits* because of transforming process, such as in the pediment, bajada, bottom of valleys, and beach sediments **(Harraz., 2013)**. **Fig (11)**

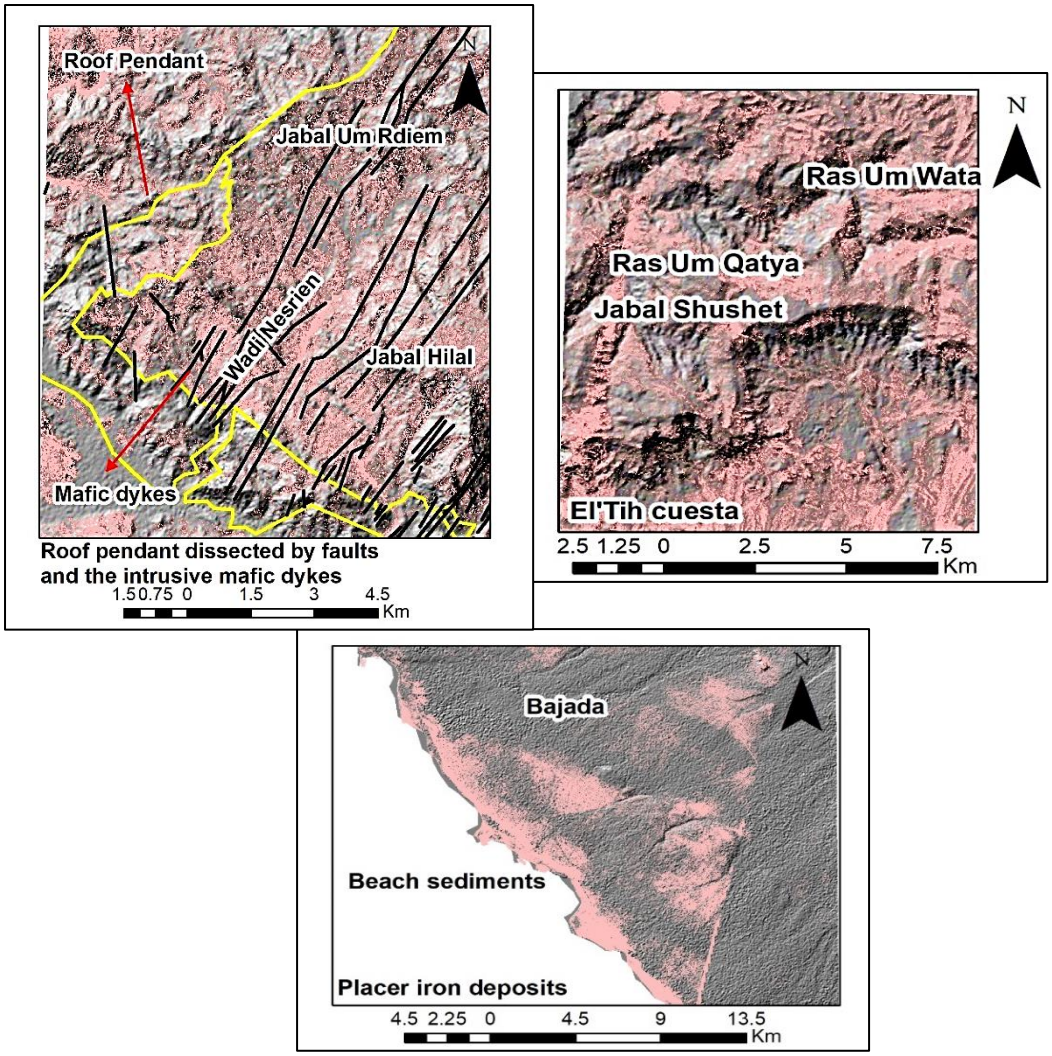


**Figure (11): Geomorphological features of iron oxide minerals**

**Source:** The studied alteration zones classified according to digital number "DN" value, and overlay on the hill-shade and the topographic map scale 1: 500,000 of the study area.

### 6.1.2. Manganese Oxide mineral:

Traced by applied the band ratio B5/B6 and the band combination (B1+B3)/B2, (B5+B7)/B6, (B3+B5)/B4 **(Rajendran & Nasir., 2013)**. Which is shown in blue color and concentration areas are blue dark tone. **Fig (12)**

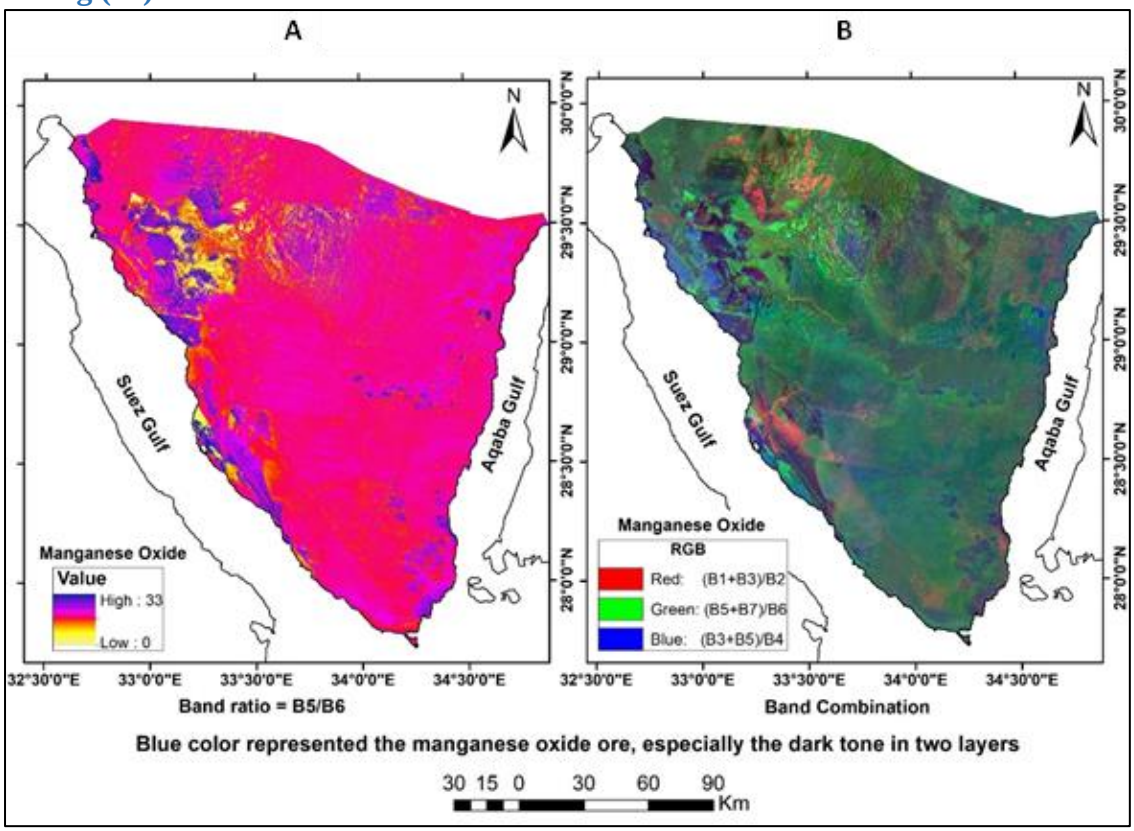


**Figure (12): Manganese oxide alternation zones in South of Sinai**

**Source:** according to apply the band ratio and the band combination methods.

***Geological setting***, is concentrated where iron is abundant in sedimentary rocks **(Hewson, et al., 2006).** But present in a small amount in igneous rocks.

***Geomorphological features,*** appear as fibers, cracked needles, and a massive form. It is found in lenses, veins and layered deposits interbedded the iron where the stratiform of sandstone and clay **(Pirajno., 1992).** Also, appears in the folded mountains and as ancient weathering and erosion products of the rock's crust. **Fig (13)**

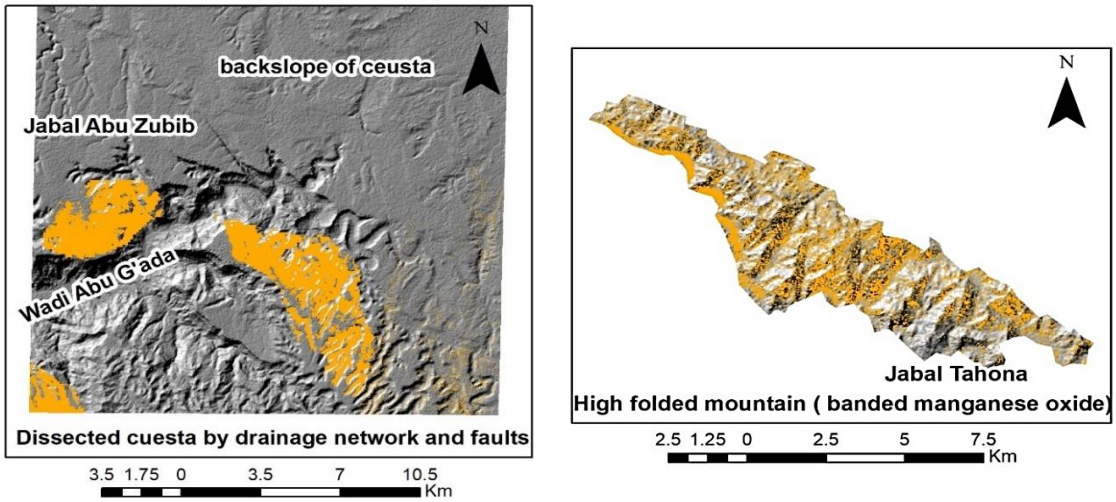


**Figure (13): Geomorphological features of manganese oxide mineral**

**Source:** overlaying the highest DN value of manganese oxide zones on the hill-shade of the study area.

## 6.2. Carbonate minerals:

Widespread in the sedimentary rocks as Calcite, Dolomite, Magnesite, Aragonite, and Siderite minerals, which are rich in $CO_3$. **(Rafferty., 2012)** Concentrated in the geological contact area of Eocene-Cretaceous and Miocene-Cretaceous rocks.

***Calcite*** recognized by using the band ratio (B7+B9)/B8 and the PCA3.**Table (8) & Fig (15-A&D)** ***Dolomite*** identified by using the band ratio (B6+B8)/B7 and the PCA3.**Table (9) &Fig (15-B&E)** ***Magnesite*** traced by the band ratio (B6+B8)/(B7+B9) **(Khunsa. et al.,2017)** and the PCA3. **Table (10) & Fig (15-C&F)** ***Carbonate minerals*** depending on the JPL, areas of mix alteration zones "calcite, dolomite, and magnesite" can be traced. By applying the principal component analysis on bands 8, 4, 9, and 6 on one side. And the band combination of Calcite (R): PCA3, Dolomite (G): PCA3, and Magnesite (B): PCA3 on the other side. **Fig (14) & Table (11) & Fig (15-G&H)**

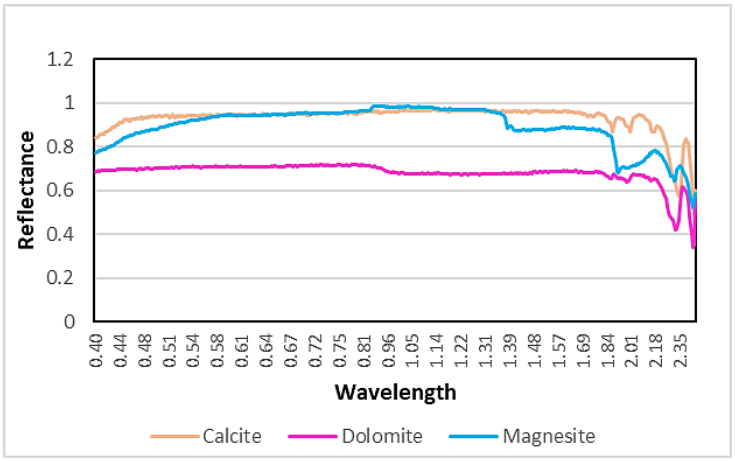


**Figure (14): Spectral signature of Carbonate minerals from JPL library**

**Table (8): Eigenvalues and Eigenvectors of PCA's Calcite**

| PCA | Band 7 | Band 8 | Band 9 |
|---|---|---|---|
| 1 | 0.57811 | - 0.2823 | - 0.76557 |
| 2 | 0.57754 | - 0.52121 | 0.62832 |
| 3 | 0.5764 | 0.80538 | 0.13828 |

**Table (9): Eigenvalues and Eigenvectors of PCA's Dolomite**

| PCA | Band 6 | Band 7 | Band 8 |
|---|---|---|---|
| 1 | 0.57622 | -0.71225 | 0.40084 |
| 2 | 0.57908 | 0.0097 | -0.81522 |
| 3 | 0.57675 | 0.70186 | 0.41803 |

**Table (10): Eigenvalues and Eigenvectors of PCA's Magnesite**

| PCA | Band 6 | Band 7 | Band 8 | Band 9 |
|---|---|---|---|---|
| 1 | 0.49936 | -0.6255 | -0.4176 | 0.43012 |
| 2 | 0.50151 | 0.09648 | -0.3525 | -0.78417 |
| 3 | 0.49962 | 0.74367 | -0.06365 | 0.43964 |
| 4 | 0.49951 | -0.21539 | 0.83505 | -0.08242 |

**Table (11): Eigenvalues and Eigenvectors of PCA's Carbonate minerals**

| PCA | Band 8 | Band 4 | Band 9 | Band 6 |
|---|---|---|---|---|
| 1 | 0.51737 | 0.79677 | 0.2464 | 0.19179 |
| 2 | 0.49311 | 0.49792 | 0.69612 | 0.15601 |
| 3 | 0.49475 | 0.00518 | 0.50523 | 0.70707 |
| 4 | 0.49436 | 0.34237 | 0.4466 | 0.66252 |

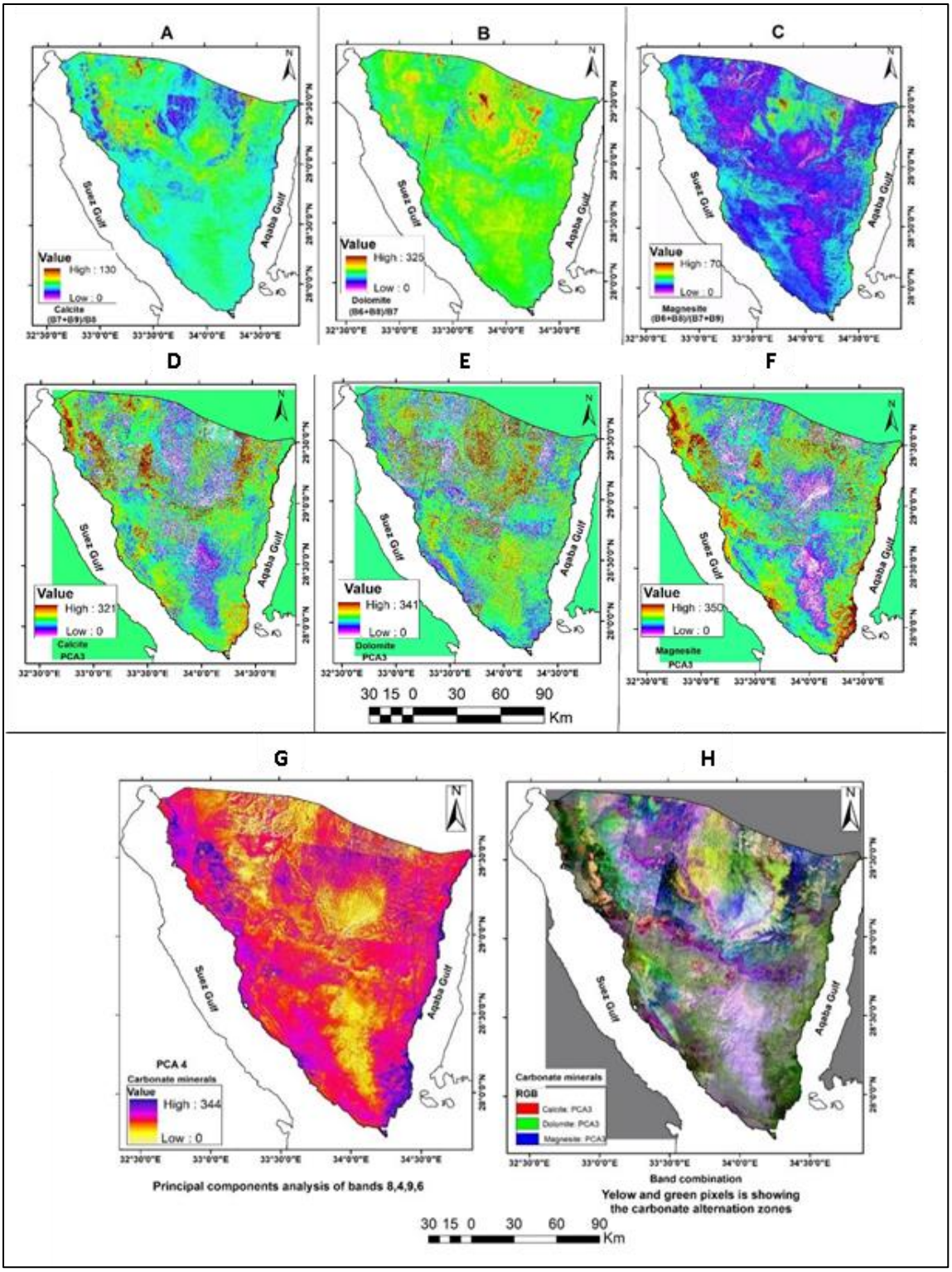


**Figure (15): Carbonate alteration zones in the South of Sinai**

***Geological setting:***

***6.2.1.*** ***Calcite*** appears in limestone, marble, as a small part of the earth's crust by the magma process and cementation material of sandstone.

***6.2.2.*** ***Dolomite*** is a product of the replacement process of calcite in the limestone by the rainfall reaction. Occurred as dolostone, dolomite marble, and dolomite carbonatite in igneous rock **(Yaxley. et al., 2022).**

***6.2.3.*** ***Magnesite*** is an element in the calcite groups, produced in the calcite rock due to the magnesium-bearing solutions, in an ultramafic metamorphic environment, serpentine shear zone, and the carbonation action of olivine in the presence of carbon dioxide and the availability of water **(Scheller. et al., 2021, Hermann. 2022).**

***Geomorphological features*****:** carbonate minerals appear in the karst landforms particularly in the sinkholes and underdrainage by the deposition process in the sedimentary rocks. In particular, calcite has a low resistance to chemical weathering. Therefore, it breaks down, dissolves, and moves from one place to another by groundwater solutions and surface water **(Singhal & Gupta, R. 2010)**. Also, carbonates appear as small plugs, dikes, sills, breccias, and veins in the igneous rocks **(Embabi, 2018)** that form when carbonate magma that is rich in CO3 – thanks to sodium, calcium, and sometimes potassium - separates from and intrudes into the alkalic igneous rocks. Besides, carbonates appear in the medium and high-folded mountains in ultramafic rocks. **Fig (16)**

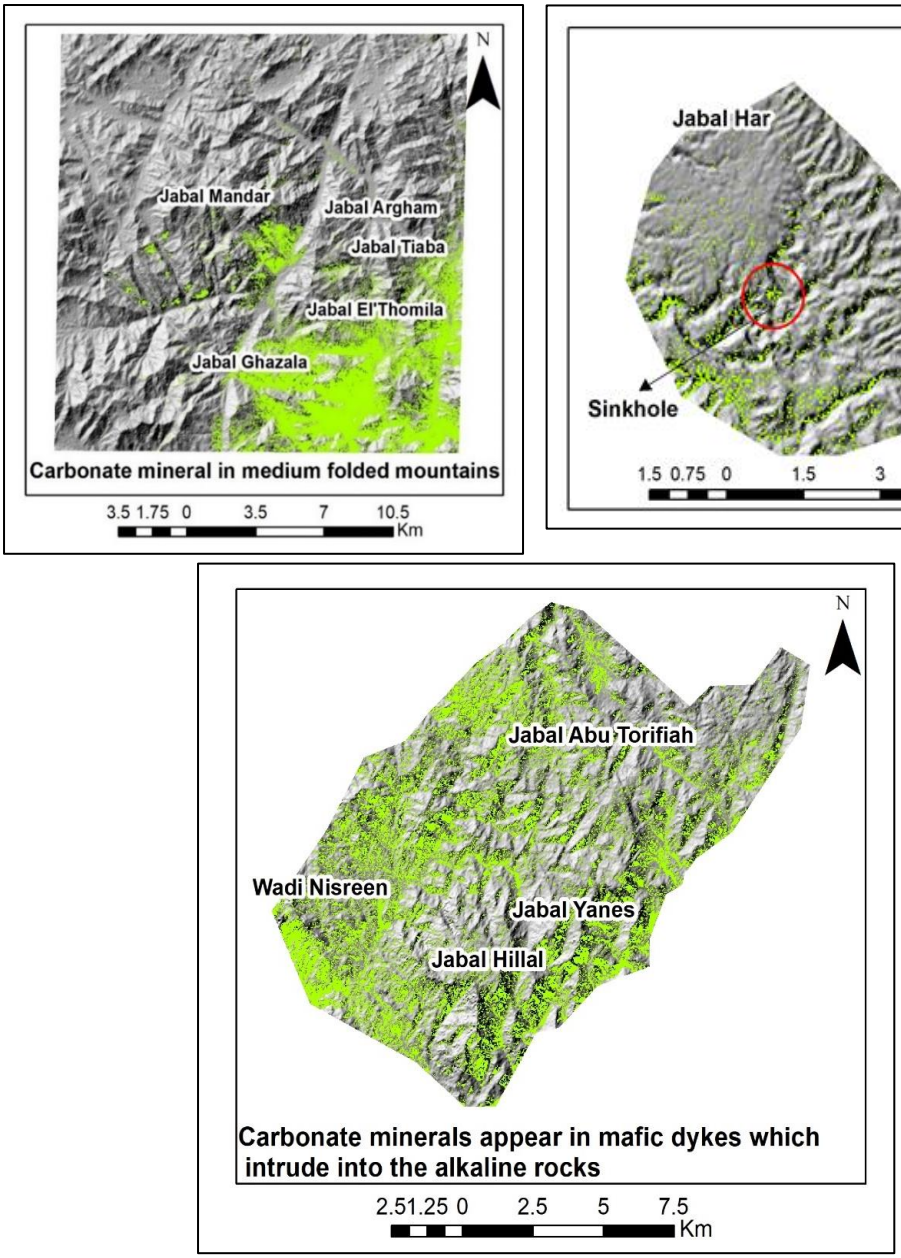


**Figure (16): Geomorphological features of carbonate minerals**

**Source:** overlaying the highest DN value of the carbonate minerals zones on the hill-shade.

The term ***(manganolites)*** refers to the manganese ore in carbonate and oxide minerals. **Fig (NO.17)**

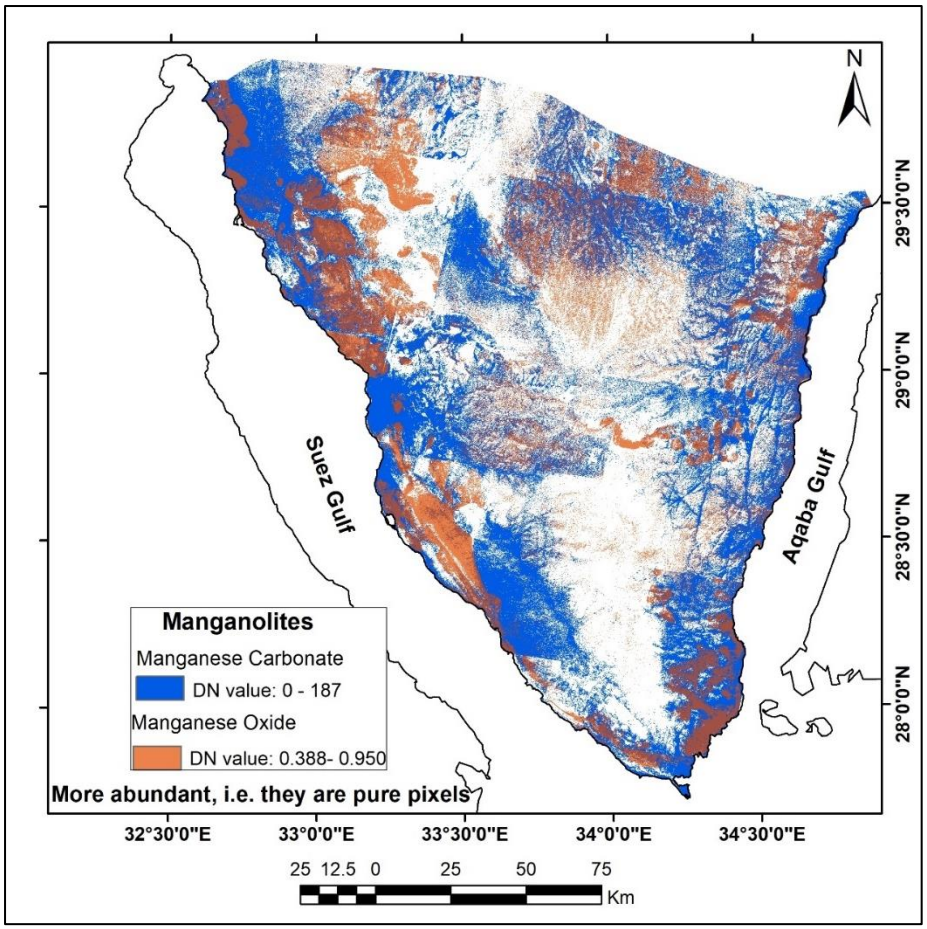


**Figure (17): Manganolites alteration zones in the South of Sinai**

**Source:** extracting the highest digital number "DN" value of manganese minerals zones.

## 6.3. Clay minerals:

Appear in three alteration mineralization zones which are argillic, propylitic and phyllic. Propylitic zones including chlorite, epidote and amphibole. Phyllic zones containing illite, muscovite, smectite and sericite **(Damian., 2003)**. Argillic zones contain alunite, kaolinite and montmorillonite minerals **(Abubakar & Hashim., 2017).**

- Traced the propylitic zones by (B7+B9)/B8 and B5/B8, phyllic zones by (B5+B7)/B6 and B5/B6 **(Salem, et al., 2018)**, argillic zones by (B4+B6)/ B5 and B5/B6, B7/B6, B7/B5 **(Alkashghari, et al., 2020)**
- The principal component analysis was applied to the three alterations individually. By studying each alteration according to its spectral signature for the minerals it commonly contains and using JPL to determine its reflection and absorption bands. To determine the highest correlation value between the bands. The ***propylitic alteration*** that 5 and 9 are the reflectance bands while 7 and 8 are the absorption bands. PCA2 is the highest value correlation between bands 5 and 7. **Fig (18) & Table (12 & 13) & Fig (21- 1)**. The ***phyllic alteration*** that 4 and 5 are the reflectance bands while 7, 6, and 8 are the reverse. PCA4 is the highest value correlation between bands 7 and 8. **Fig (19) & Table (14 & 15) & Fig (21- 2)**. The ***Argillic alteration*** that 3, 4, and 7 are the reflection while 5, 6, and 9 are the absorption. PCA 6 is the highest value between 4 and 6 bands. **Fig (20) & Table (16 & 17) & Fig (21- 3)**
- The band combination propylitic (R): PCA2, phyllic (G): PCA4, and Argillic (B): PCA6 determine the clustered areas of the three alterations. **Fig (21- 4)**

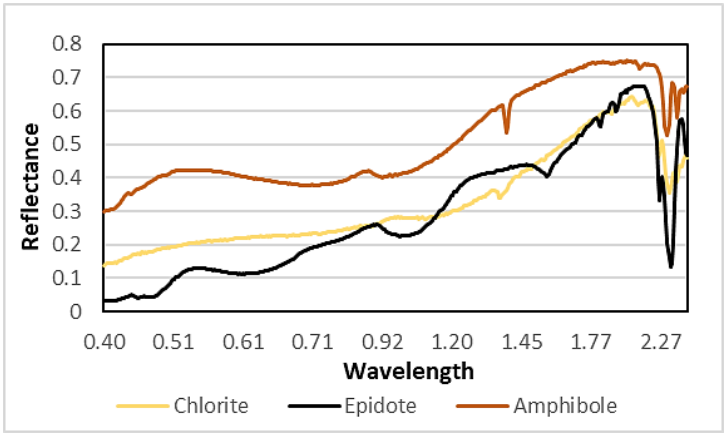


**Figure (18): Spectral signature of Propylitic minerals from JPL library**

**Table (12): reflectance and absorption bands of propylitic minerals**

| Bands | Chlorite | Epidote | Amphibole |
|---|---|---|---|
| Band 5 | Ref | Ref | ——— |
| Band 7 | Abs | Abs | Ref |
| Band 8 | Abs | Abs | Abs |
| Band 9 | Ref | Ref | Ref |

**Table (13): Eigenvalues and Eigenvectors of PCA's Propylitic minerals**

| PCA | Band 5 ↑ | Band 7 ↓ | Band 9 ↑ | Band 8 ↓ |
|---|---|---|---|---|
| 1 | 0.49177 | -0.33595 | -0.47862 | -0.64515 |
| 2 | 0.51962 | -0.62079 | 0.42784 | 0.40195 |
| 3 | 0.49473 | 0.40982 | -0.52802 | 0.55542 |
| 4 | 0.49335 | 0.57776 | 0.55595 | -0.33723 |

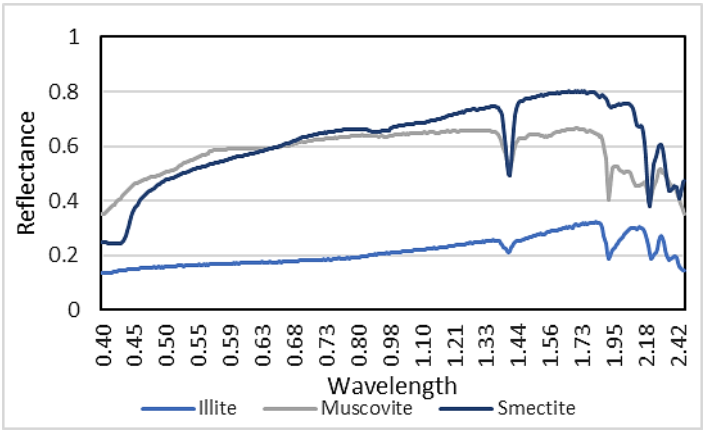


**Figure (19): Spectral signature of Phyllic minerals from JPL library**

**Table (14): reflectance and absorption bands of Phyllic minerals**

| Bands | Illite | Muscovite | Smectite | Sericite |
|---|---|---|---|---|
| Band 4 | Ref | ——— | Ref | Ref |
| Band 5 | Ref | Ref | ——— | ——— |
| Band 6 | Abs | Abs | ——— | Abs |
| Band 7 | Ref | Ref | Ref | Ref |
| Band 8 | Abs | Abs | Abs | Abs |

**Table (15): Eigenvalues and Eigenvectors of PCA's Phyllic minerals**

| PCA | Band 4 ↑ | Band 5 ↑ | Band 6 ↓ | Band 7 ↑ | Band 8 ↓ |
|---|---|---|---|---|---|
| 1 | 0.46478 | 0.62824 | 0.56267 | -0.26902 | -0.01793 |
| 2 | 0.4401 | 0.36071 | -0.43502 | 0.69612 | -0.04873 |
| 3 | 0.44414 | -0.06837 | -0.53962 | -0.55103 | 0.45082 |
| 4 | 0.44465 | -0.37371 | -0.06209 | -0.18164 | -0.79106 |
| 5 | 0.44195 | -0.57521 | 0.44622 | 0.32622 | 0.41022 |

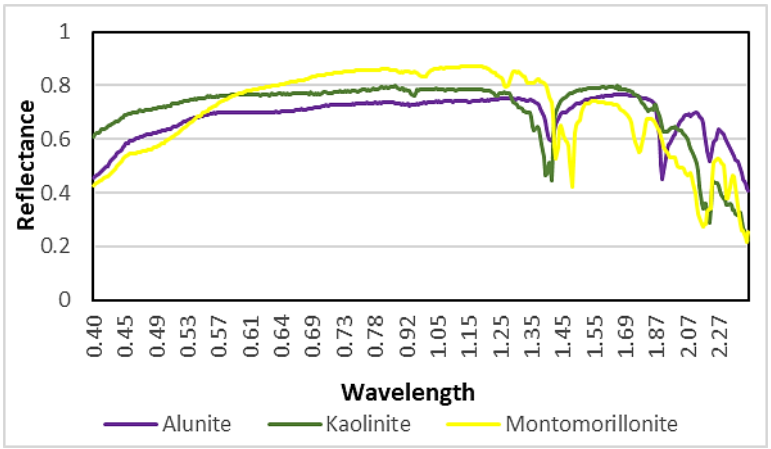


**Figure (20): Spectral signature of Argillic minerals from JPL library**

**Table (16): reflectance and absorption bands of Argillic minerals**

| Bands | Kaolinite | Montmorillonite | Alunite |
|---|---|---|---|
| Band 3 | ——— | Ref | Ref |
| Band 4 | Ref | ——— | Ref |
| Band 5 | Abs | ——— | Abs |
| Band 6 | ——— | Abs | ——— |
| Band 7 | Ref | Ref | Ref |
| Band 8 | ——— | ——— | ——— |
| Band 9 | Abs | Abs | Abs |

**Table (17): Eigenvalues and Eigenvectors of PCA's Argillic minerals**

| PCA | Band 3 ↑ | Band 5 ↓ | Band 4 ↑ | Band 6 ↓ | Band 7 ↑ | Band 9 ↓ | Average |
|---|---|---|---|---|---|---|---|
| 1 | 0.41109 | 0.8965 | 0.11573 | 0.02368 | 0.11474 | -0.01324 | **0.262497** |
| 2 | 0.40069 | -0.28799 | 0.26472 | -0.4744 | 0.66269 | 0.14907 | **0.37326** |
| 3 | 0.42352 | -0.24949 | 0.68219 | 0.42025 | -0.34059 | 0.01962 | **0.355943** |
| 4 | 0.4053 | -0.11801 | -0.20062 | -0.38748 | -0.33111 | -0.72235 | **0.360812** |
| 5 | 0.40522 | -0.06542 | -0.37213 | -0.23134 | -0.44053 | 0.66743 | **0.363678** |
| 6 | 0.40325 | -0.18137 | -0.52194 | 0.62779 | 0.35774 | -0.09989 | **0.36533** |

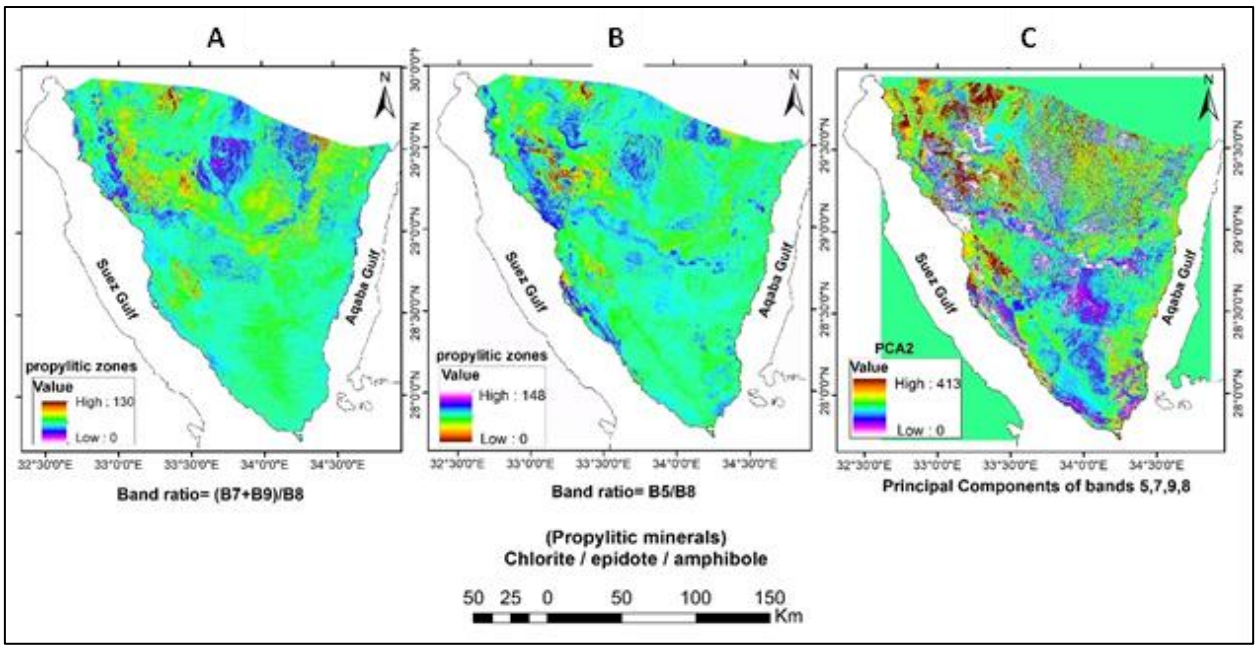


**Figure (21-1): Propylitic alteration zones in the South of Sinai**

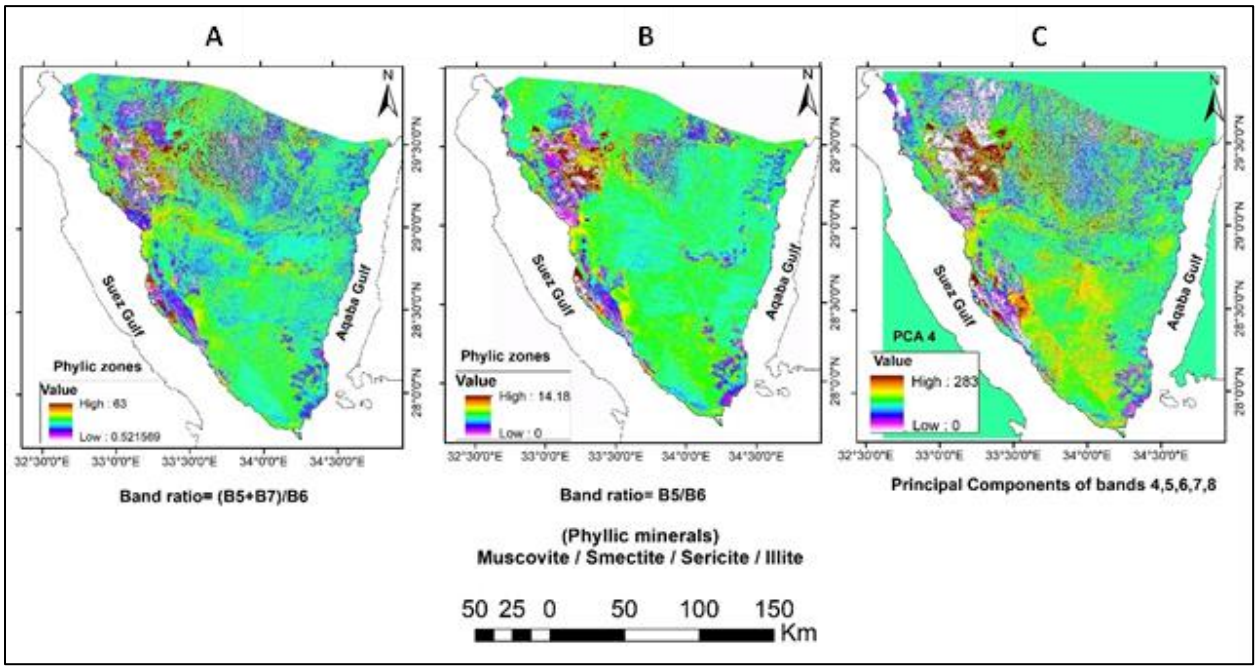


**Figure (21-2): Phyllic alteration zones in the South of Sinai**

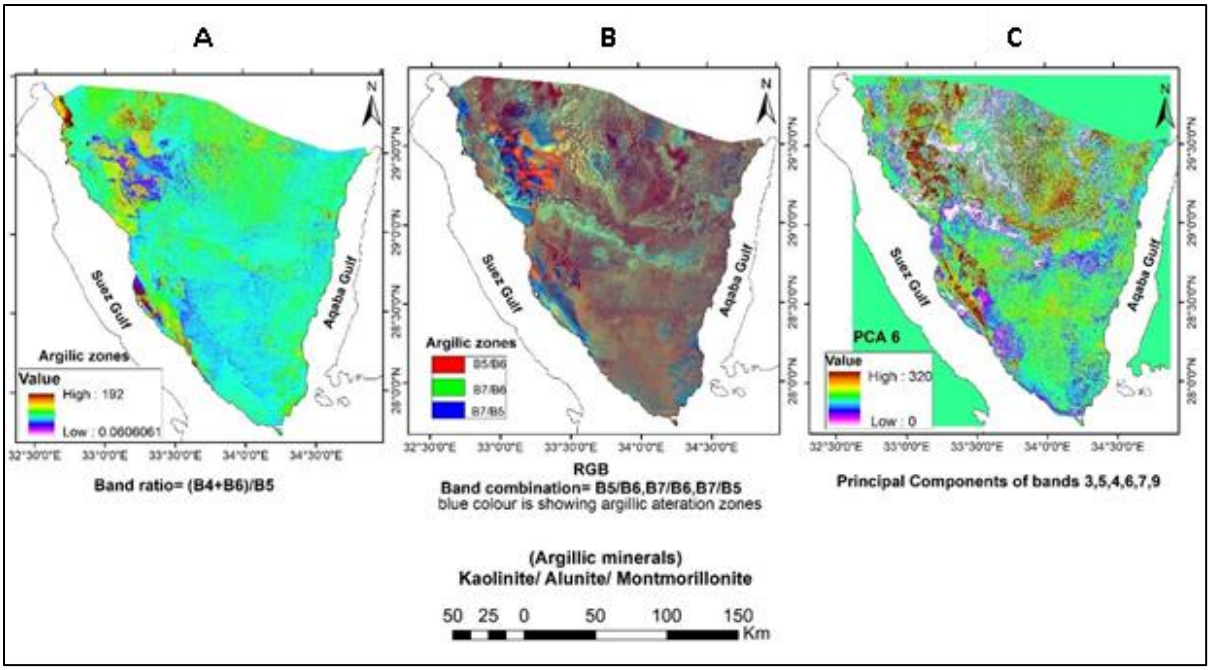


**Figure (21-3): Argillic alteration zones in the South of Sinai**

**Source:** applying three methods "band ratio, band combination, and principal components analysis".

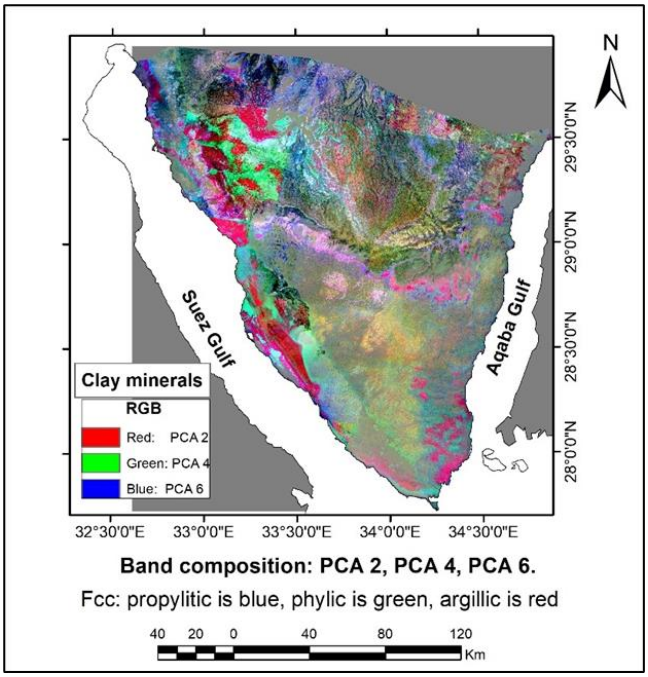


**Figure (21-4): Clay minerals alteration zones in the South of Sinai**

**Source:** aggregating the highest DN values of the PCA of propylitic, phyllic, and argillic alteration zones in the study area.

***Geological setting:***

6.3.1. ***Propylitic zones***, *chlorite-epidote* is common in metavolcanic such actinolite schist and chlorite-biotite schist rocks, *amphibolite* is common in metasediment as graywacke **(Hermina, et al., 1989),** in the oldest granite that contains high percent of amphibolite and plagioclase such as granodiorite **(Pirajno., 1992)**, and in the sedimentary rocks rich in marl as Glala, Esna, Rudays and Abu Alaqa formations.

6.3.2. ***Phyllic zones*** rich in calc-alkaline rocks, especially the quartz-diorite and permeable sedimentary rocks composed of calcite, and some of it is in alkaline rocks **(Pirajno., 1992)**. For example; *Illite* is a product of weathering and hydrothermal processes where there are muscovite and feldspar. *Muscovite* occurred in igneous rocks as granites and pegmatite, in metamorphic rocks as gneiss, schist, and phyllite, and in sedimentary rocks which derived from the previous rocks. *Smectite* is the hydrous aluminum silicate resulting from the weathering reaction of basic rocks, volcanic rich in silica and hydrothermal alterations environment. *Sericite* is the white mica or fine-grained muscovite that formed in hydrothermal alternations in plagioclase and orthoclase feldspar available. Common in the low-grade metamorphic rocks **(Kumari & Mohan., 2021).**

6.3.3. ***Argillic zones*** are more abundant in the igneous rocks as granodiorite, monzogranite and synogranite **(Parry, W.2002),** volcanic rocks such dacite and syenite, metamorphic rocks as metamorphosed acid volcanic, and sedimentary rocks as Eocene, Miocene, and Cambrian rocks. *Kaolinite* mineral appears in igneous rocks thanks to their content of quartz and orthoclase feldspar. And in sedimentary rocks thanks to their sandstone content. Which results from the decomposition by chemical weathering. *Montmorillonite* mineral is common in areas of volcanism and late hydrothermal activity with bentonite was formed during the Cretaceous Period. *Alunite* mineral occurred in the advanced argillic alteration. **(Thompson, et al., 1996).** It's a sulfate mineral formed in an acid solution **(Pirajno., 1992)**. Appears in many types of rocks especially the volcanic rocks such as andesite, dacite, rhyolite, and trachyte.

***Geomorphological features: Propylitic zones*** in the medium dissected mountains, high folded mountains, clitters and northwestern folds and its deposits appear on the bed of karstic valleys and at the foot of the topographic escarpment **Fig (22).** ***Phyllic zones*** occurred as bands in the low-grade metamorphosed rocks as in the case of *illite*. As gentle slopes and low-density drainage such as smectite. Exists in veins as *sericite*. Mechanical weathering affects the drainage network consisting of *schist*, making the valley floor winding and low levels as a trap for clay mineral deposits. In general, phyllic zones concentrated in the low slope's areas of the high folded mountains, domes, high weathered batholite plutons, and dissected plateau **Fig (23).** ***Argillic zones*** appear in high slopes of hogbacks, Eocene folds, high dissected plateaus, and the top of domes. It concentrated in the conspicuous ridges and shade places. Or formed as massive, veins, gaps of rocks and intense leaching as alunite **(Pirajno., 1992)**. **Fig (24)**

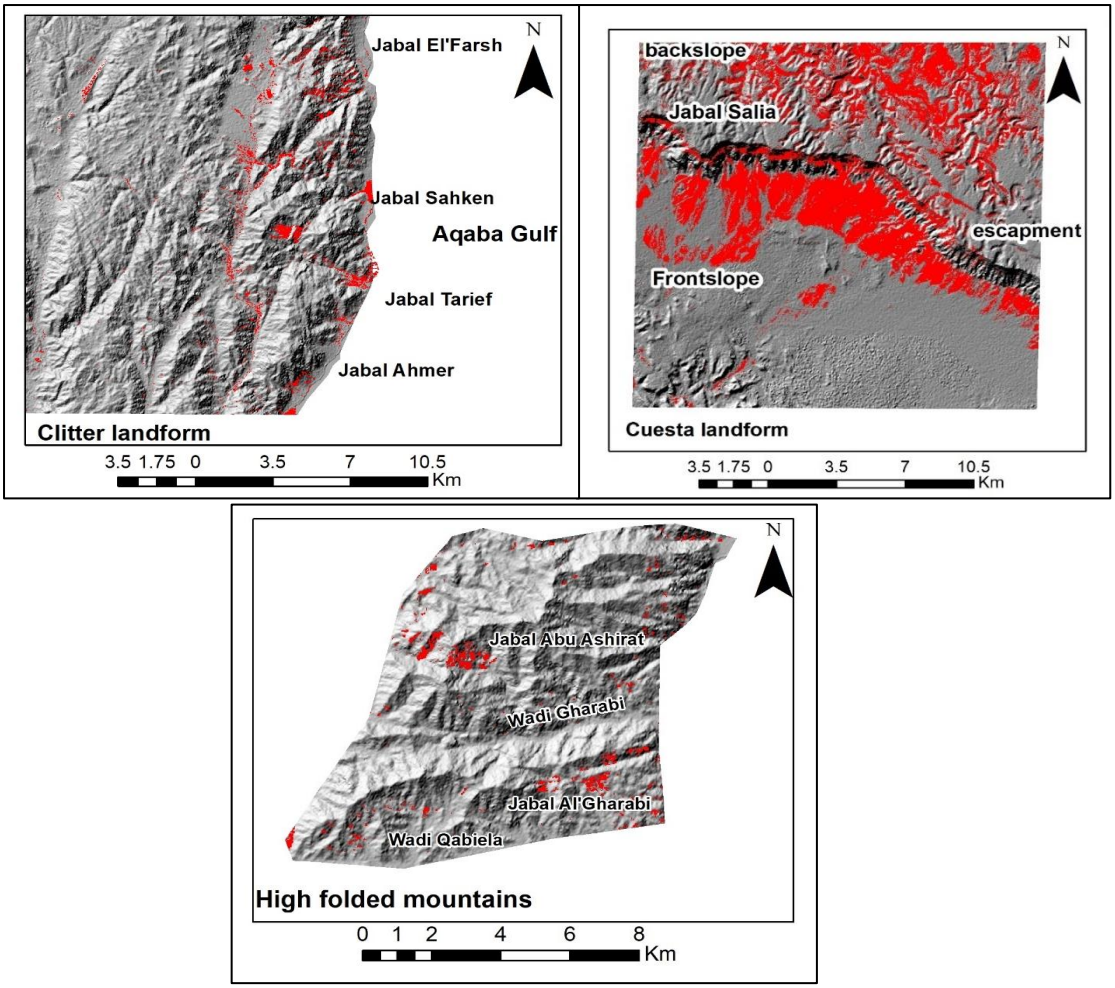


**Figure (22): Geomorphological features of propylitic zones**

**Source:** overlaying the highest DN value of the propylitic zones on the hill-shade.

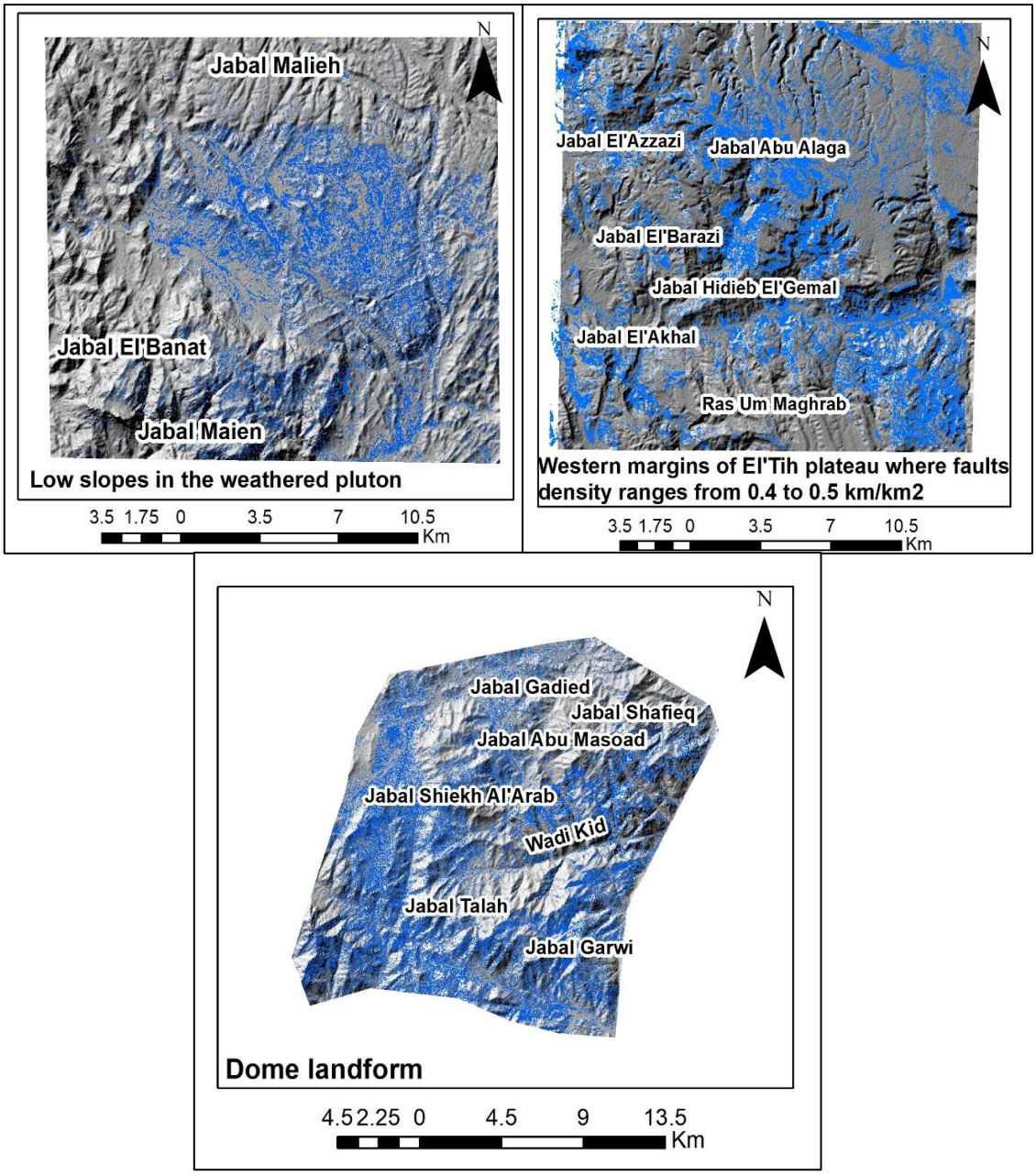


**Figure (23): Geomorphological features of phyllic minerals**

**Source:** overlaying the highest DN value of the phyllic zones on the hill-shade.

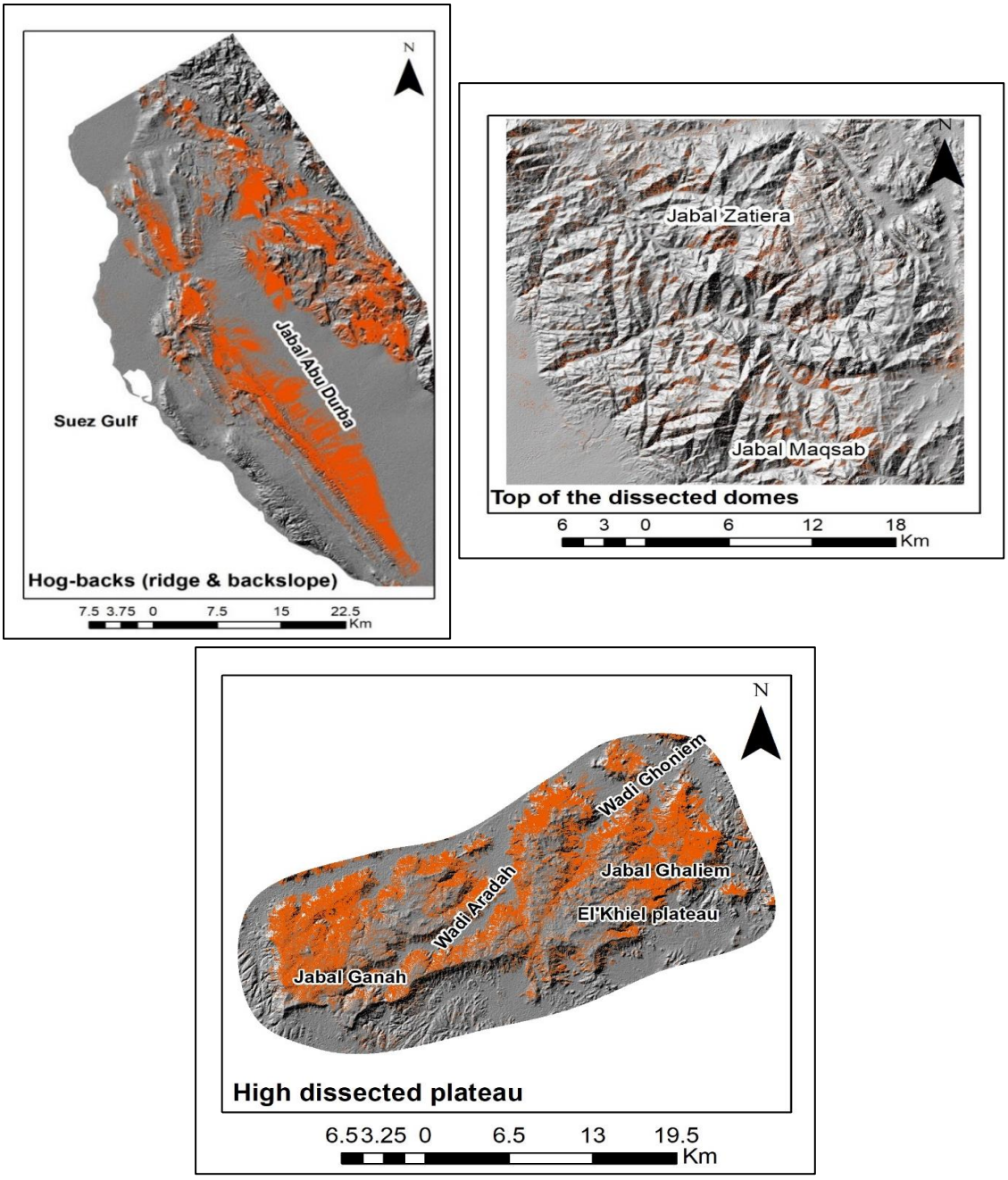


**Figure (24): Geomorphological features of argillic minerals**

**Source:** overlaying the highest DN value of the argillic zones on the hill-shade.

## 6.4. Sulfide minerals:

Containing economic and industry minerals such as gold, copper, zinc, lead, marcasite, and galena. Traced in the study area depending on the band combination B12, B5, B3 **(Alkashghari, et al., 2020)**. Also, the principal component analysis was applied with the help of JPL to determine the study bands, which showed a high correlation in PCA3 between bands 3 and 5. **Fig (25) & Table (18) & Fig (26)**

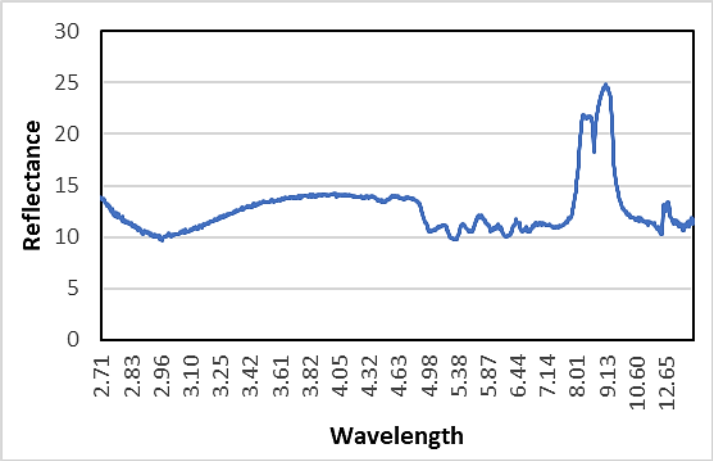


**Figure (25): Spectral signature of Sulfide minerals from JPL library**

**Table (18): Eigenvalues and Eigenvectors of PCA's Sulfide minerals**

| PCA | Band 3 | Band 5 | Band 12 | Average |
|---|---|---|---|---|
| 1 | 0.60079 | -0.36831 | -0.70951 | **0.559537** |
| 2 | 0.56237 | -0.43606 | 0.70256 | **0.566997** |
| 3 | 0.56815 | 0.8211 | 0.05485 | **0.481367** |

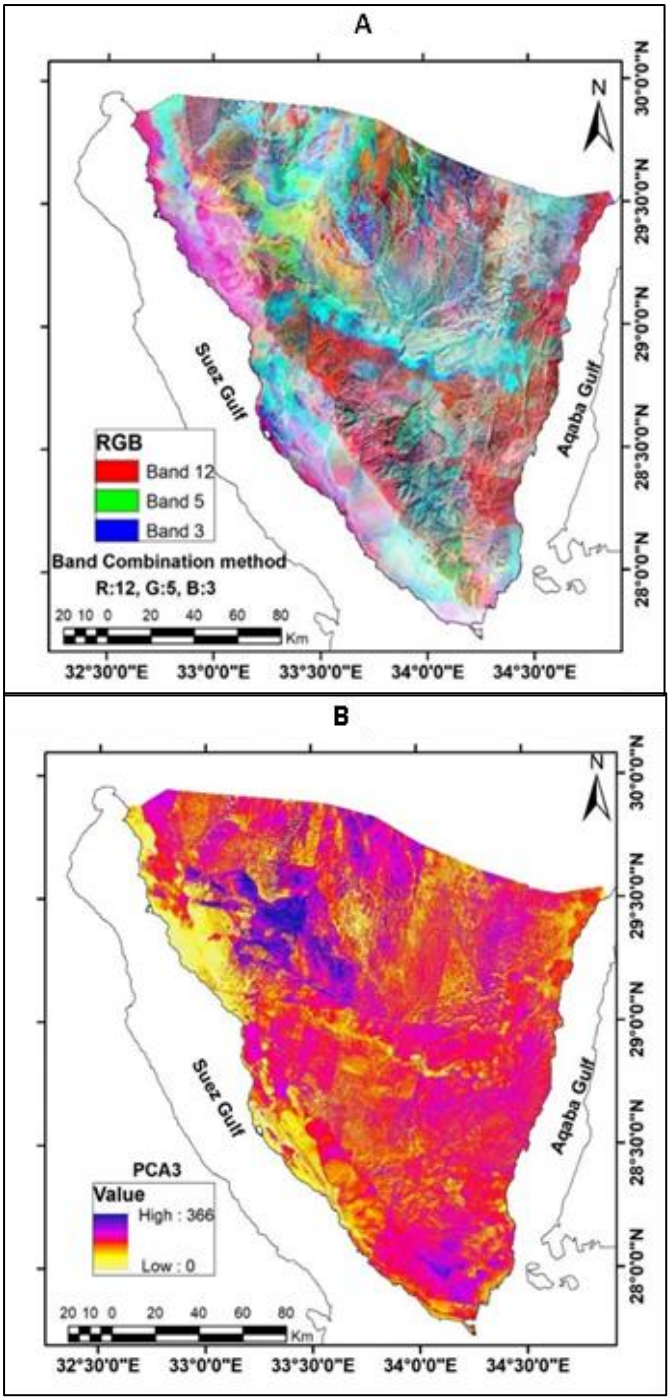


**Figure (26): Sulfide alteration zone in the South of Sinai**

**Source:** applying two methods; band combination and principal components analysis.

***Geological occurrence,*** formed in the initial crystallization process of the mafic magma and the deposition process in the salt solutions under high temperature and pressure. Occurred in all rocks but concentrated in the volcanic rocks, in the high permeability sedimentary rocks, and in the hydrothermal deposits which are closely related to igneous intrusion as porphyry granophyre. **(Faisal, et al., 2021)**

***Geomorphological features,*** occur in the veins and joints of limestone and gypsum as isolated bodies. In the faults and fractures filling of granites, particularly the alkaline type. Concentrated in the dissected landforms where fault density ranges from 1:0.5 to 1: 0.7 km/km$^2$. **Fig (27)**

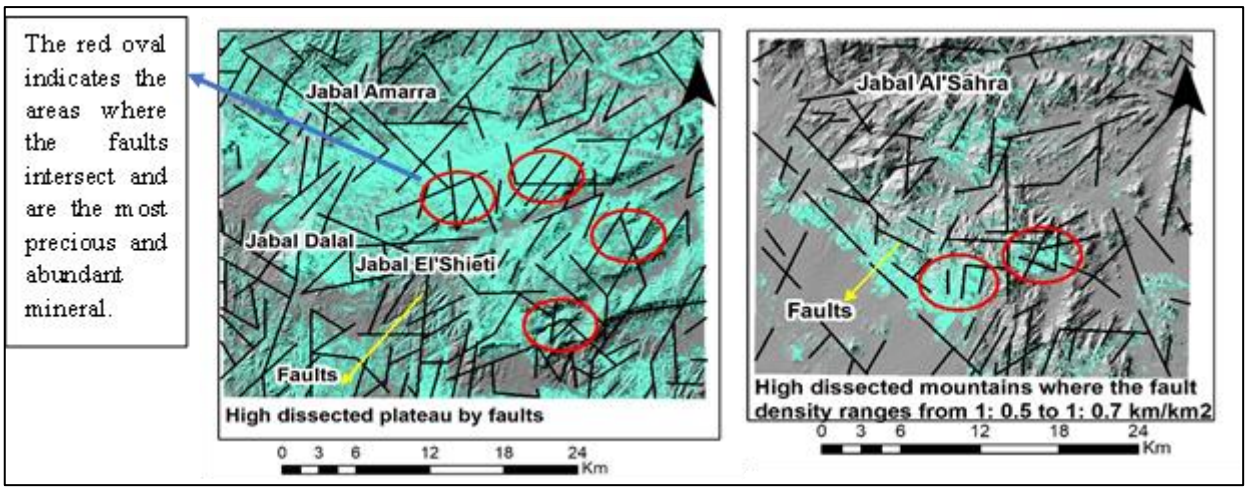


**Figure (27): Geomorphological features of sulfide minerals**

**Source:** overlaying the highest DN value of the sulfide zones on the hill-shade

## 6.5. Silica and Silicate minerals:

They are common minerals because involved in many mineral compositions such as quartz, feldspar, mica, amphibole, pyroxene, olivine, and garnet. Appear obviously in TIR bands by applying three methods to reach the most concentrated areas of silica minerals. The band ratio B13/B10, B14/B12, and B13/B14 **(Oha, et al., 2021).** The band composite of these band ratios. The principal component analysis is between five bands, namely 10, 12, and 14 as reflectance bands and 11 and 13 as absorption bands. The results show that PCA2 is the highest grade between 13 and 12 bands. **Fig (28) & Table (19) & Fig (29)**

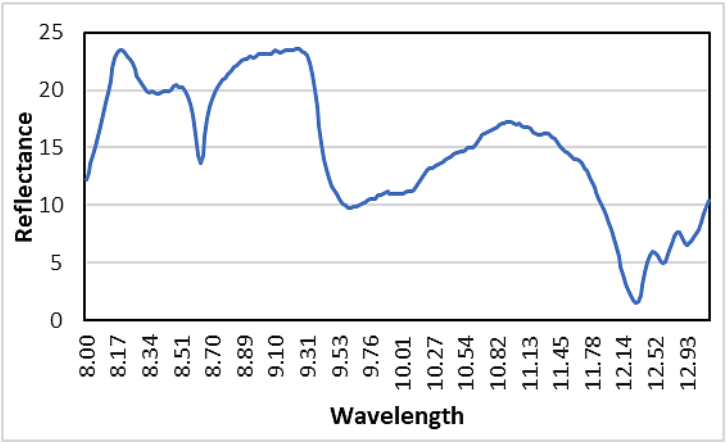


**Figure (28): Spectral signature of Quartz minerals from JPL library**

**Table (19): Eigenvalues and Eigenvectors of PCA's Silica minerals**

| PCA | Band 11 | Band 10 | Band 13 | Band 12 | Band 14 | Average |
|---|---|---|---|---|---|---|
| 1 | 0.45028 | -0.28745 | -0.19035 | -0.80526 | 0.17305 | **0.6725** |
| 2 | 0.45028 | -0.29422 | -0.67512 | 0.49409 | -0.1038 | **0.716948** |
| 3 | 0.44502 | 0.5008 | 0.10851 | -0.11157 | -0.7259 | **0.667716** |
| 4 | 0.44816 | -0.48903 | 0.70179 | 0.25978 | 0.00234 | **0.670808** |
| 5 | 0.44228 | 0.58383 | 0.06082 | 0.16583 | 0.65752 | **0.675656** |

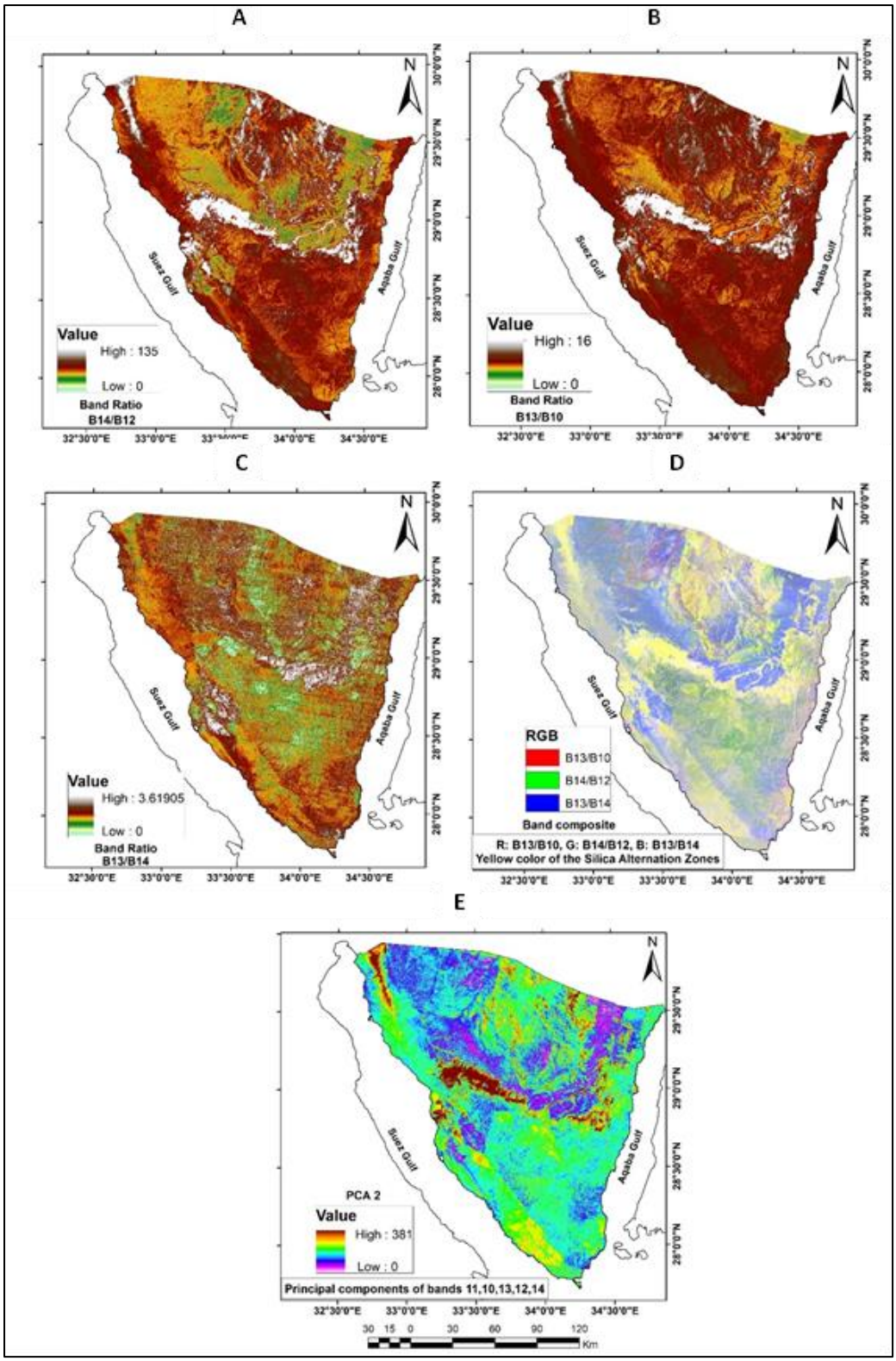


**Figure (29): Silica and Silicate alternation zones in South of Sinai**

***Geological occurrence,*** silica ore is abundant in igneous rocks rich in quartz and feldspar such as granites, quartz is a pure silica. Besides, the silicification process occurs in sedimentary rocks represented in sandstone which belong to Cambrian and Eocene rocks, especially below massive sulfide deposits **(Thompson, et al., 1996)**.

***Geomorphological features***, silicification, and silcretes occurred in the plutons, quartz domes, and rugged lands which were dissected by swarms of dykes (as weathered products). And appear as white color veins in igneous and metamorphic rocks. Residual silica appears as bodies that termed vuggy silica or as deposits in alluvial, colluvial deltas, bottom of valleys, beaches, and plains **(Kumari & Mohan., 2021, Hedenquist, et al., 2000)**. **Fig (30)**

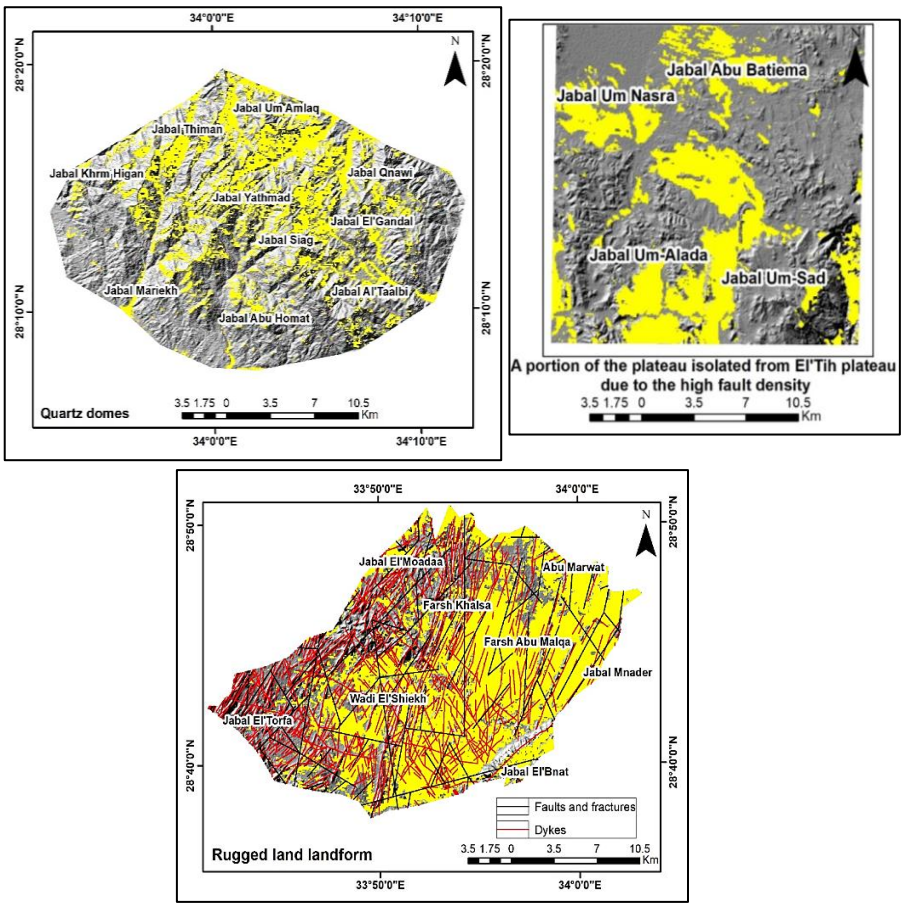


**Figure (30): Geomorphological features of silica minerals**

**Source:** overlaying the highest DN value of silica zones on the hill-shade.

## 6.6. More-abundant alteration mineral zones and the promising areas:

The final eight mineral alteration zones were classified into two categories, less and more-abundant. Depending on the DN value of the histogram by using the "Reclassify Tool" in the ArcGIS program. This method is a manual pure pixel process. **Fig (31)**

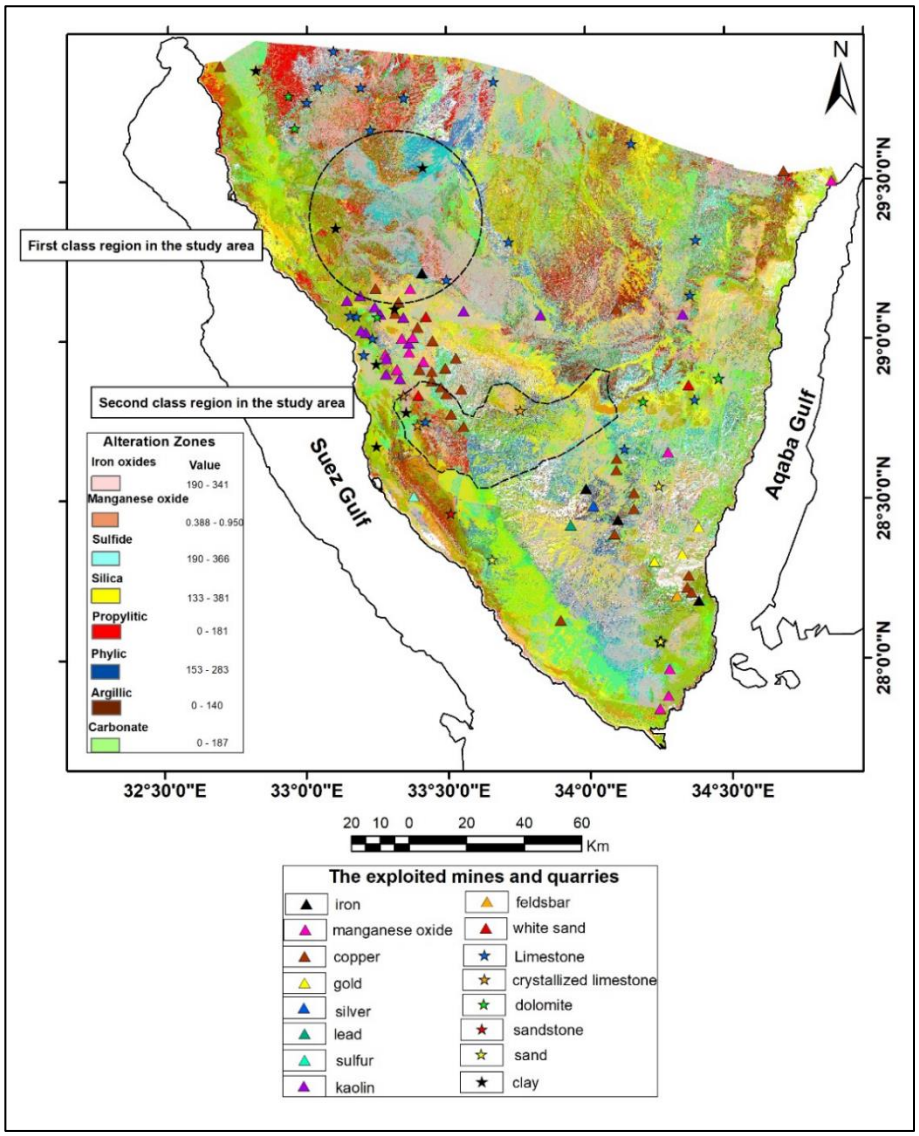


**Figure (31): Distribution of the more-abundant alteration zones in South of Sinai**

**Source:** extracting and overlaying the more-abundant alteration mineral zones of the study area.

Noticed, from the results obtained, that East Ras Malaab and Wadi feiran are one of the most diverse and rich in minerals. By comparing the results and the currently exploited mines, Abu Zneima is the most exploited area. So, Southwestern Sinai is the promising area in the region.

## 6.7. The road network that serves the south of Sinai:

The road network has been studied based on the Atlas of Egypt Roads, and it has been updated with the help of the "Open Street Map". **Fig (32)** The length of each road category has been calculated and its shapes studied. **Table (20) & Fig (33)**

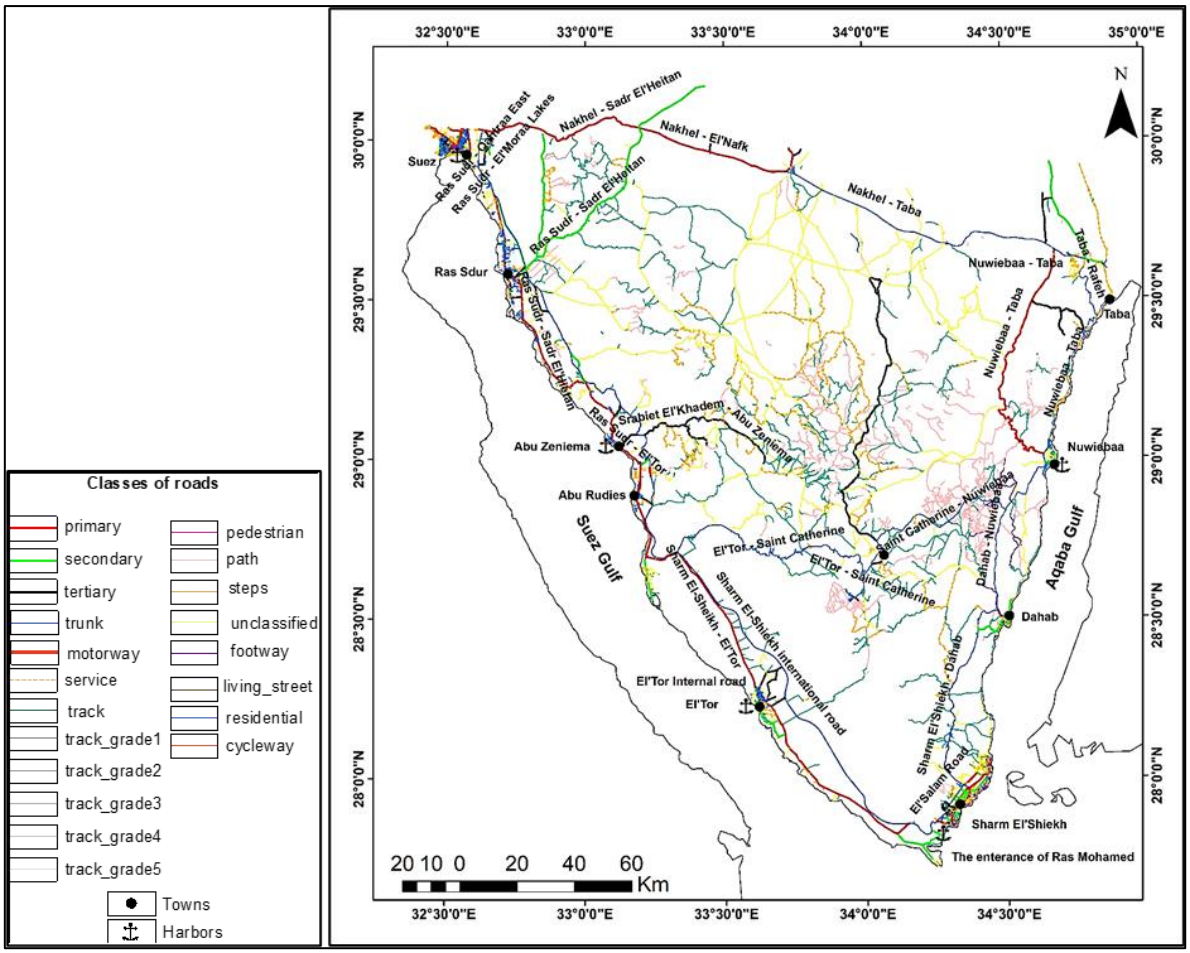


**Figure (32): The road network in Southern Sinai**

**Source:** updated the road network map scale 1: 420.000 according to Open Street map.

**Table (20): Length of the road network according to its classes**

| Type | classification | Length (km) | Length % |
|---|---|---|---|
| Paved roads | Primary | 935.59 | 5.97 |
| | Secondary | 683.69 | 4.36 |
| | Tertiary | 593.80 | 3.79 |
| | Trunk | 1514.56 | 9.66 |
| | **Total** | **3727.64** | **23.78** |
| Paved roads for citizens | Service | 2126.75 | 13.57 |
| | Motorway | 11.72 | 0.07 |
| | Track | 2566.17 | 16.37 |
| | Track grade1 | 3.20 | 0.02 |
| | Track grade2 | 7.12 | 0.05 |
| | Track grade3 | 18.45 | 0.12 |
| | Track grade4 | 3.70 | 0.02 |
| | Track grade5 | 19.05 | 0.12 |
| | Residential | 2064.10 | 13.17 |
| | Cycleway | 12.72 | 0.08 |
| | Footway | 374.23 | 2.39 |
| | Living street | 21.37 | 0.14 |
| | **Total** | **7228.58** | **46.12** |
| Unpaved roads | Steps | 6.47 | 0.04 |
| | Path | 2370.04 | 15.12 |
| | Pedestrian | 29.59 | 0.19 |
| | Unclassified | 2315.32 | 14.77 |
| | **Total** | **4721.42** | **30.12** |
| | **General total** | **15677.64** | **100** |

**Source:** analyzing the road network and applying some measurements.

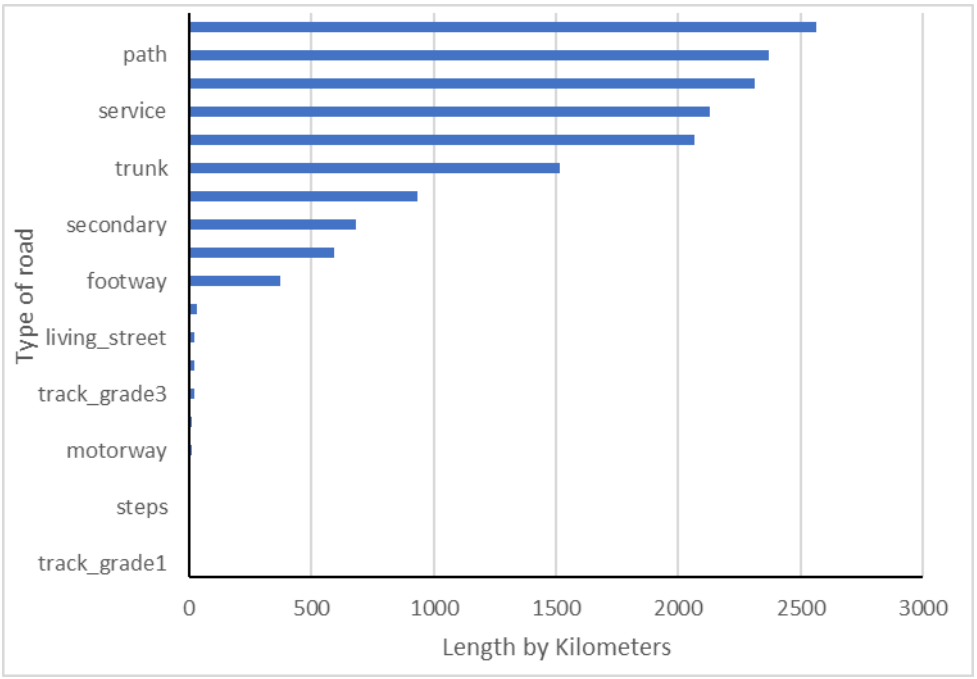


**Figure (33): The length of roads types in the South of Sinai**

**Source:** represent the data in table (20) graphically by using EXCEL application.

The availability of a good road network is the basis for the mining process, especially the paved roads. From studying the road network map, the following was observed:

- Because of the complex geographical nature of the study area, which limits the availability of paved roads, the alternative was to have unclassified roads, paths, and tracks.
- The road network density in South Sinai includes paved and unpaved roads: $\boldsymbol{Density\ of\ roads} = \frac{\boldsymbol{Legnth\ of\ roads}}{\boldsymbol{arae\ of\ region}} \times \mathbf{100}$

$$\boldsymbol{Density\ of\ roads\ in\ Southern\ Sinai} = \frac{\mathbf{15677.64\ km}}{\mathbf{31780\ km2}} \times \mathbf{100} = \mathbf{49.33\%}$$

- The density of paved roads suitable for heavy vehicles; (primary, secondary, tertiary, and trunk):

$$\boldsymbol{Density\ of\ paved\ roads\ in\ Southern\ Sinai} = \frac{\mathbf{3727.7\ km}}{\mathbf{31780\ km2}} \times \mathbf{100} = \mathbf{11.73\%}$$

- Unpaved roads represent 30.12% of the total road lengths, paved roads that do not serve the research point represents 46.12%, and paved road suitable to minerals transport is 23.78%. **Table (20) & Fig (33)**

- The road network is concentrated at the outskirts of the study area due to the flat and plain land, but it is internal roads serving the human which are classified as residential and living streets. **Fig (32)**
- There are roads in the region called circuits, which are several segments and nodes of roads connected, forming a closed circle. Making it easy to get to and from.
- There are three circular routes. The wider circle is an indicator of the more rugged area, due to the difficulty of extending an internal road network. The widest ring roads surround the plateaus of Sinai, then the circle surrounding the southern mountainous triangle, and finally the circle linking Taba with Nuweibaa. Shown obviously in **Figure (34).**
- The roads were studied in terms of the closest distance depending on the "Euclidean Distance" tool, which will be dealt with in more detail later. **Fig (34)**
- There are five harbors in the region., one in the east "Nuweibaa", three in the west "Suez, Abu Zneima, and El'Tor", and one in the south "Sharm El'Sheikh".

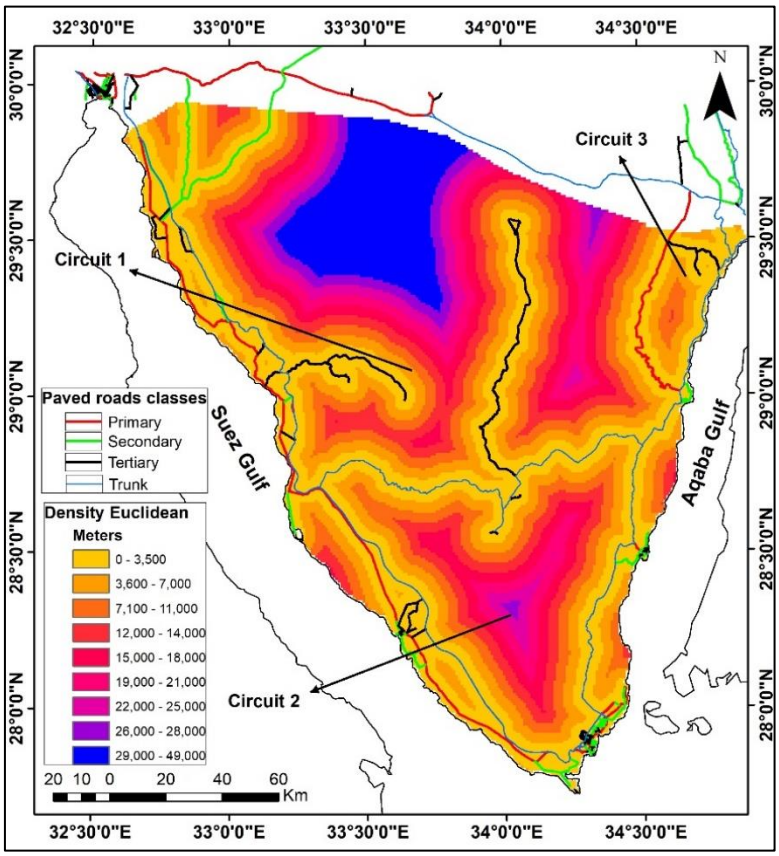


**Figure (34): The Euclidean Distance of paved roads in the South of Sinai**

**Source:** using Euclidean density tool in ARCGIS program on the paved roads.

## 6.8. Case study:

According to the results of studying the more abundant mineralization alteration zones in the South of Sinai and overlaying it on the exploited mines and quarries now. Consequently, it determined the two most promising areas in the study area; the first area is east of Ras Al-Mallab and the second area is Wadi Feiran. It will study each area separately.

### 6.8. 1. First region:

It is located to the **east of Ras Al-Mallab**, especially the Wardan and Grendel basins, and small parts of Al-Arish, Wasit, Al-Himyar and Sieh basins. Its area is 2,817 $km^2$. Most of the area consists of Cretaceous rocks and is characterized by a high density of faults, folds and shear zones. The region is a part of Al-Ajma Plateau where occupies the southwestern side, and includes many landforms and geomorphological features such as mountain peaks, valleys, springs, and wells. The road network covering the area is unpaved, but it is close to the port of Abu Zenima, which serves the area. It was possible to determine the locations of the mineralization areas in the study area, according to the overlaying method of the alteration zones, the topographic map at a scale of 1:50,000, the density of faults and fractures, and the lithology and geomorphological map. Therefore, only mountainous areas were mentioned in the **Table (21)** because they contain minerals of high economic value, and valleys and springs were excluded, despite their importance, but they contain minerals in lower percentages. Accordingly, Mount Malbad is the most important in the region and is considered a promising mineral area. **Fig (35)**

**Table (21): distribution of mineralization alteration zones in the East Ras Malaab area**

| Iron Oxide | Manganese | Carbonate | Propylitic | Phyllic | Argillic | Sulfide | Silica |
|---|---|---|---|---|---|---|---|
| J. Malbad | J. Abu Zubub | J. El Abyad | J. Malbad | J. Abu Alaga | J. Malbad | J. Malbad | J. El Gushiya |
| J. El Azzazi | Ras Um Maghrab | J. Umm Kitheira | J. El Azzazi | J. El Barazi | J. Umm Helwa | J. Azzazu | J. Gorlos |
| J. El Akhal | J. El'Iseila | J. Kreir | J. El Barazi | J. El Akhal | J. El Abiad | J. El Barazi | J. El Iseila |

| | | | | | | | |
|---|---|---|---|---|---|---|---|
| J. Abu Lasafa | J. Umm Helwa | J. Gorlos | J. Abu Alaga | J. El Gushiya | J. Umm Kithera | J. Abu Alaga | Ras Umm Qatafa |
| El Iseila | J. El Barazi | J. El Tihiya | J. El Akhal | Ras Umm Qatafa | J. Krier | J. Abu Zubub | Western J. El Ratma |
| J. El Ratama | J. El Tihiya | Abu Ideimat | J. Abu Lasafa | J. Ras Wata | J. Abu Lasafa | J. El Akhal | Ras El Azrac |
| J. Abu Zubub | J. Aneiza | South J. Megmar | Naqb Rakna | J.Sarabiet El'Gamal | Abu Ideimat | J. Abu Lasafa | J. Sarabiet El'Gamal |
| J. Abu Alaga | J. Dahhak | ———— | J. Dahak | Western J. Aneiza | J. El Tihiya | J. El Ratma | ———— |
| J. Ras Wata | ———— | ———— | J. Krier | J. Abu Lasafa | J. El Iseila | J. El Isela | ———— |
| J. Megmar | ———— | ———— | El Sinafa | ———— | J. Aneiza | Ras Um Qatafa | ———— |
| ———— | ———— | ———— | ———— | ———— | J. Dahak | J. Ras Wata | ———— |
| ———— | ———— | ———— | ———— | ———— | J. El Azzazi | J. Aneiza | ———— |
| ———— | ———— | ———— | ———— | ———— | ———— | J. Magmar | ———— |

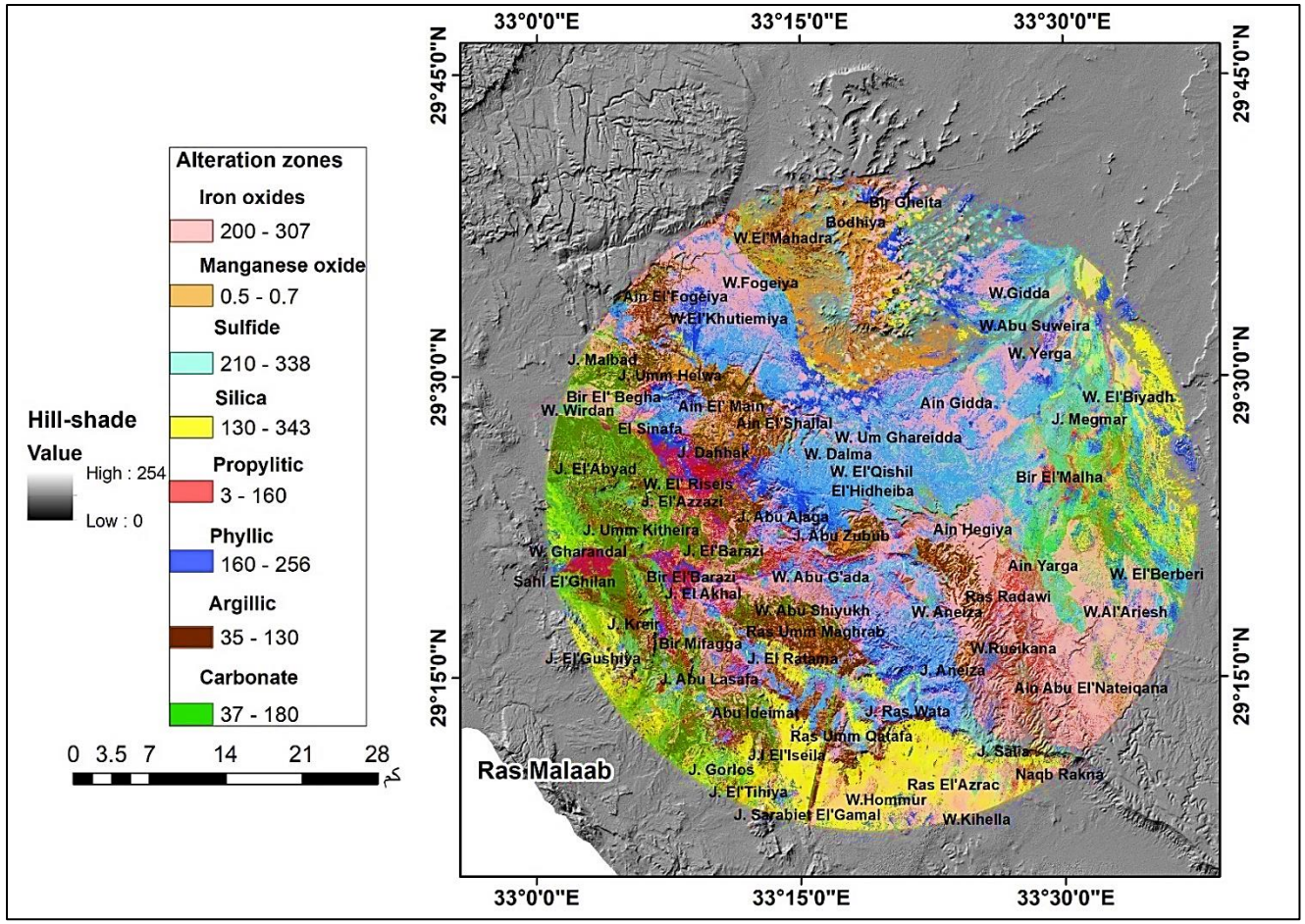


**Figure (35): the mineralization alteration zones sites in the East Ras Malaab**

### 6.8.2. Second region:

Located along **Wadi Feiran**, particularly Wadi Um Lusiefa, Al-Akhdar, Al-Sheikh, and Solaf. Also, parts of Wadi Al-Awaag and Watier. Its area is 1.780 km2. The western side is composed of igneous rocks as Granodiorite, monzogranite, and Alkaline granite, metamorphic rocks such as gneiss, metagabbro, and metadiorite. The eastern side consists of sedimentary rocks such as Cretaceous, small parts of Eocene and Miocene rocks. The area enjoys the swarms of felsic and mafic dykes and shear zones beside it receives large amounts of rainfall annually. All of these factors encouraged a high rate of weathering and the availability of groundwater, thus forming hydrothermal solutions. The area consists of mountains interspersed with wadies, rugged lands which are highly dissected by geological structures so some parts are presented as plains covered by sand sheets, and hogback landforms.

A second-class paved road passes through the south of the area, which serves the mining process, but there are no ports close to its coast. It's noticed that the western side which is close to the Suez coast is more abundant in minerals, especially Mount Hadahed. In addition, Serbal, Srabiel, and Maktab are the richest mountain areas of minerals in the basement rocks region. **Fig (36) Table (22)**

**Table (22): distribution of mineralization alteration zones in Wadi Feiran**

| Iron Oxide | Manganese | Carbonate | Propylitic | Phyllic | Argillic | Sulfide | Silica |
|---|---|---|---|---|---|---|---|
| J.Mander | J. Maktab | J. Maktab | J. Maktab | South J.Aqnah | J. Maktab | J.Mander | J. Serbal |
| J. Al Banat | South J. Al Banat | J. Gozah | J. Esiah | J. Al Banat | J. Gozah | J. Al Banat | J. Ganah |
| J. Homra | J. Homra | J. Torfa | J. Al Tor | J. Homra | J. Torfa | J. Aborah | J. Al Banat |
| J. Hadahed | J.Hadahed | J. Hadahed | J. Hadahed | J. Hadahed | J.Hadahed | J. Serbal | J. Serbal |
| J. Abu Turifiah | J. Abu Turifiah | J. Abu Turifiah | Riesha Al Muweilha | West J. Turifiah | J. Abu Turifiah | J. Sedriah | J. Sedriah |
| J. Serbal | West J. Ganah | J. Tahonah | ———— | J. Sedriah | J. Om Tar | North J. Ganah | J. Samraa |

| | | | | | | | |
|---|---|---|---|---|---|---|---|
| J. Samraa | J. Al Tor | J. Ahmar | ———— | J. Serbal | J. Serbal | West J. Esiah | Farsh Al Khaiam |
| J. Matgah | J. Maien | J. Matgah | ———— | J. Orabi | J. Maien | North J. Rumaithi | Farsh Abu Malgah |
| J. Om Tar | ———— | ———— | ———— | J. Maien | West W. Kahieliea | J. Om Tar | J. Om Tar |
| Riesha Al Muweilha | ———— | ———— | ———— | J. Matgah | J. Matgah | J. Samraa | J. Homra |
| ———— | ———— | ———— | ———— | J. Srabiel | J. Srabiel | J. Taqtaqat | J. Maien |
| ———— | ———— | ———— | ———— | South JAqnah | J.Taqtaqat | J. Matgah | ———— |
| ———— | ———— | ———— | ———— | J. Samraa | J. Samraa | Al Turiefiah | ———— |
| ———— | ———— | ———— | ———— | J. Al Goz | J. Al Goz | Abu Marwat | ———— |

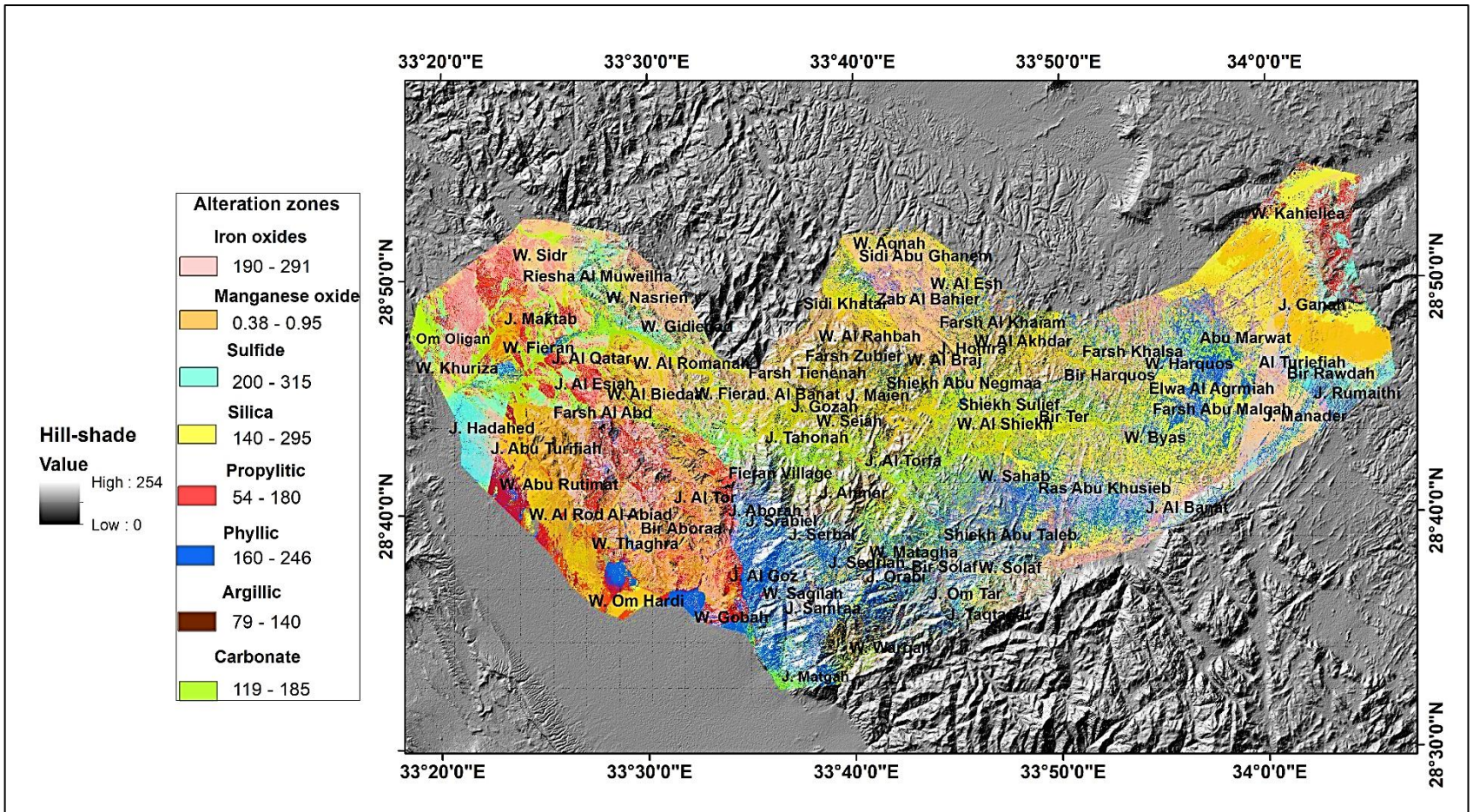


**Figure (36): the mineralization alteration zones sites in Wadi Feiran**

## 7. Conclusion:

ASTER VNIR is very sensitive in determining the iron oxide and some of sulfide minerals. ASTER SWIR is very effective in clay, carbonate, sulfide, ferrous silicate minerals, and hydrothermal alteration zones. While the relation between VNIR and SWIR bands is good to obvious some kinds of iron oxides and sulfide minerals. ASTER TIR is an effective tool in silicate minerals .The four methods used in data processing - band ratio, band combination, PCA, and classified data - were dealt with in an integrated manner in order to reach high accuracy and specific results. The using of the JPL library helps to discriminate the reflectance and absorption bands thus determining the mineral alterations.

The high density of faults and fractures, especially their junction and intersection points are one of the most important Geological determinants of the mineralization alteration zones. Besides, the rock types surrounding the area and the formation of mineral deposits derived from the same rocks on which they are concentrated. Therefore, the mineral alteration zones varied according to the lithology in the region. For example: Iron oxides derived from the sandstone and ophiolite rocks, carbonates from limestone and dolomite, and silica from alkali granite. As a result, the landforms differ according to the minerals they contain. This is an essential matter that helps to easily identify and guide to the locations of minerals in the field. For example: sinkholes and blind valleys are evidence of the presence of carbonates. Granite domes indicate the presence of quartz. The conspicuous ridges include many economic minerals such as zinc, nickel, manganese, and copper. The rugged land which is highly weathered is an important source of sand. The gently sloping lands of the dissected plutons show phyllic alteration. While argillic alterations appear in ridges and backslopes of hogbacks.

The road network is essential to the development of minerals. However, the roughness of the terrain led to the difficulty of establishing a paved road network, so most of them are unpaved roads which represented 30.12% of the total road length. It is characterized by the presence of circuit roads that facilitate the transportation process inside the region and a number of ports that help transport goods outside it.

Southwestern Sinai is the richest mineral area in the region. East of Ras al-Malaab and Wadi Feiran are promising areas. While the Abu Zneima area and the southeastern region are the most exploited areas now.

## 8. Recommendations:

1. The region needs more studies to detect the minerals.
2. Geomorphologists should pay attention to mineral geomorphology by conducting further studies.
3. The trend toward designing maps linking landforms and geomorphological features to mineral distribution.
4. The concern for the development of the road network.
5. Overcoming obstacles to access minerals more easily by constructing bridges.

## Acknowledgment:

I would like to express my special thanks of gratitude to ***Dr. Fathi Hassan*** the geophysics professor in the Faculty of Science, at Alexandria University. Which supported, and gave me the power to finish this work and review the research paper.

## References:

Abdelhalim, Ahmed & Aboelkhair, Hatem & Hamimi, Zakaria & Al-Gabali, Majid. (2020). Mapping lineament features using GIS approaches: case study of Neoproterozoic basement rocks in the South-Eastern Desert of Egypt. Arabian Journal of Geosciences. 13. 10.1007/s12517-020-05673-4.

Aboelkhair, H., Abdelhalim, A., Hamimi, Z. et al (2020). Reliability of using ASTER data in lithologic mapping and alteration mineral detection of the basement complex of West Berenice, Southeastern Desert, Egypt. Arab J Geosci 13, 287. https://doi.org/10.1007/s12517-020-5227-x

Abrams, & Yamaguchi, Yasushi. (2019). Twenty Years of ASTER Contributions to Lithologic Mapping and Mineral Exploration. Remote Sensing. 11. 1394. 10.3390/rs11111394.

Abu El-Enen, Mahrous & Whitehouse, Martin. (2013). The Feiran–Solaf metamorphic complex, Sinai, Egypt: Geochronological and geochemical constraints on its evolution. Precambrian Research. 239. 10.1016/j.precamres.2013.10.011.

Abubakar, Aliyu & Hashim, Mazlan. (2017). Identification of hydrothermal alteration minerals associated with geothermal system using ASTER and

Hyperion satellite data: a case study from Yankari Park, NE Nigeria. Geocarto International. 34. 1-57. 10.1080/10106049.2017.1421716.

Adabi, Mohammad & Akbari, & Rasa, Zabeh & Mohajel, I. & Yarmihamadi. (2015). Hydrothermal Alteration of Ahangaran Deposits, West of Iran Using ASTER Spectral Analysis. International Geoinformatics Research and Development.

Ali-Bik, Mohamed & Gabr, Safwat & Hassan, Safaa. (2022). Spectral characteristics, petrography and opaque mineralogy of the Oligo-Miocene basalts at Wadi Abu Qada- Wadi Wata area, west-central Sinai, Egypt. Egyptian Journal of Remote Sensing and Space Science. 25. 10.1016/j.ejrs.2022.02.005.

Alkashghari, Wadee & Matsah, Mohamed & Baggazi, Haitham & EL-Sawy, El-Sawy & Elfakharani, Abdelhamid & El-Shafei, Mohamed. (2020). Detection of alteration zones using ASTER imagery and geological field observations: Al Wajh area, Northwestern Arabian Shield, Saudi Arabia. Arabian Journal of Geosciences. 13. 10.1007/s12517-020-05818-5.

Anovitz, Lawrence & Cheshire, Michael & Hermann, Raphaël & Gu, Xin & Sheets, Julia & Brantley, Susan & Cole, David & Ilton, Eugene & Mildner, David & Gagnon, Cedric & Allard, Lawrence & Littrell, Kenneth. (2021). Oxidation and associated pore structure modification during experimental alteration of granite. Geochimica et Cosmochimica Acta. 292. 532-556. 10.1016/j.gca.2020.08.016.

Cengiz, O. & Şener, Erhan. (2019). International Journal of Multidisciplinary Studies and Innovative Technologies Investigation of the Applicability of ASTER Satellite Images for Exploration of Barite Mineralization in the Bitlis Region.

Cudahy, Thomas & Okada, Kazuya & Cornelius, Amanda & Hewson, Robert. (2023). Regional to Prospect Scale Exploration for Porphyry-Skarn-Epithermal mineralisation at Yerington, Nevada, using ASTER and Airborne Hyperspectral data CONTENTS.

Cudahy, Thomas. (2016). Mineral Mapping for Exploration: An Australian Journey of Evolving Spectral Sensing Technologies and Industry Collaboration. Geosciences. 6. 52. 10.3390/geosciences6040052.

Damian, Floarea. (2003). The mineralogical characteristics of the hydrothermal types alteration from Nistru ore deposit, Baia Mare metallogenetic district. Studia Universitatis Babes-Bolyai, Geologia. 48. 10.5038/1937-8602.48.1.9.

Di Tommaso, Ines & Rubinstein, Nora. (2007). Hydrothermal alteration mapping using ASTER data in the Infiernillo porphyry deposit, Argentina. Ore Geology Reviews - ORE GEOL REV. 32. 275-290. 10.1016/j.oregeorev.2006.05.004.

El-Bialy, Mohammed & Ali, Kamal. (2013). Zircon trace element geochemical constraints on the evolution of the Ediacaran (600–614 Ma) post-collisional Dokhan Volcanics and Younger Granites of SE Sinai, NE Arabian–Nubian Shield. Chemical Geology. 360–361. 54–73. 10.1016/j.chemgeo.2013.10.009.

El-Desoky, Hatem & Shebl, Ali & Abdel-Rahman, Ahmed & Fahmy, Wael & El-Awny, Hamada & El-Sherif, Anas & El-Rahmany, Mahmoud & Csámer, Árpád. (2022). Multiscale mineralogical investigations for mineral potentiality mapping of Ras El-Kharit-Wadi Khashir district, Southern Eastern Desert, Egypt. Egyptian Journal of Remote Sensing and Space Science. 25. 941-960. 10.1016/j.ejrs.2022.09.001.

Elkazzaz, Yahia. (2012). SHEAR ZONES RELATED GOLD-BEARING QUARTZ VEINS IN SHINAI AREA, SOUTH EASTERN DESERT, EGYPT. Egyptian Journal of Geology. 56. 67-89.

El-Masry, Nabil & El-Kaliouby, Baher & Khawasik, Samir & El-Ghawaby, Mohamed. (1992). Reconstruction of the Geological Evolution of Saint Catherine Ring Dyke, South Sinai. Proceedings 3nd Conference Geology Sinai Development, Ismailia.

El-Qassas, R.A.Y., Abu-Donia, A.M. & Omar, A.E.A. Delineation of hydrothermal alteration zones associated with mineral deposits, using remote sensing and airborne geophysics data. A case study: El-Bakriya area, Central Eastern Desert, Egypt. Acta Geod Geophys 58, 71–107 (2023). https://doi.org/10.1007/s40328-023-00405-y

El-Sayed, Mohamed. (2006). Geochemistry and petrogenesis of the post-orogenic bimodal dyke swarms in NW Sinai, Egypt: constraints on the magmatic–tectonic processes during the late Precambrian. Chemie der Erde - Geochemistry. 66. 129-141. 10.1016/j.chemer.2003.12.003.

El-Shafei, Mohamed & Kusky, Timothy. (2003). Structural and tectonic evolution of the Neoproterozoic Feiran-Solaf metamorphic belt, Sinai Peninsula: Implications for the closure of the Mozambique Ocean. Precambrian Research. 123. 269-293. 10.1016/S0301-9268(03)00072-X.

Embabi, Nabil. (2004). The geomorphology of Egypt: Landforms and Evolution. The Nile Valley and the Western Desert. 1.

Embabi, Nabil. (2018). Landscapes and Landforms of Egypt: Landforms and Evolution. 10.1007/978-3-319-65661-8.

Faisal, Mohamed & Yang, XY & Zhang, Huishan & Amuda, Abdulgafar & Sun, Chao & Mostafa, Sara & Gul, Muhammad Amar. (2021). Mineralization Styles, Alteration Mineralogy, and Sulfur Isotope Geochemistry of Volcanogenic Massive Sulfide Deposits in the Shadli Metavolcanics Belt, South Eastern Desert,_Egypt: Metallogenic Implications. Ore Geology Reviews. 10.1016/j.oregeorev.2021.104402.

Fatima, Khunsa & Ur Rehman, Asid & Khattak, Umar & Kausar, Allah & Toqeer, Muhammad & Haider, Naghma. (2017). Minerals identification and mapping using ASTER satellite image. Journal of Applied Remote Sensing. 11. 10.1117/1.JRS.11.046006.

Forshaw, Jacob & Pattison, David. (2021). Ferrous/ferric (Fe2+/Fe3+) partitioning among silicates in metapelites. Contributions to Mineralogy and Petrology. 176. 10.1007/s00410-021-01814-4.

Fowler, Abdel-Rahman & Hassan, Imbarak & Hassan, Mahmoud. (2015). Tectonic evolution and setting of the Sa'al Complex, southern Sinai, Egypt: A Proterozoic continental back-arc rift model. Journal of African Earth Sciences. 104. 10.1016/j.jafrearsci.2015.01.008.

Gabr, Safwat & Ghulam, Abduwasit & Kusky, Timothy. (2010). Detecting areas of high-potential gold mineralization using ASTER data. Ore Geology Reviews. 59-69. 10.1016/j.oregeorev.2010.05.007.

Grangeon, S., Bataillard, P., Coussy, S. (2020). The Nature of Manganese Oxides in Soils and Their Role as Scavengers of Trace Elements: Implication for Soil Remediation. In: van Hullebusch, E., Huguenot, D., Pechaud, Y., Simonnot, MO., Colombano, S. (eds) Environmental Soil Remediation and Rehabilitation. Applied Environmental Science and Engineering for a Sustainable Future. Springer, Cham. https://doi.org/10.1007/978-3-030-40348-5_7

Guha, Arindam & vinod Kumar, Kumranchat & Porwal, Alok & Pasricha, Komal & K.C.Sahoo, & Kumar, S.RAneesh & Singaraju, Vuddaraju & R.P.Singh, & MK.Khandelwal, & Raju, P. & Diwakar, P.. (2018). Reflectance spectroscopy and ASTER based mapping of rock-phosphate in parts of Paleoproterozoic sequences of Aravalli Group of rocks, Rajasthan, India. Ore Geology Reviews. 108. 10.1016/j.oregeorev.2018.02.021.

Harraz, Hassan. (2013). Placer Mineral Deposits. 10.13140/RG.2.1.3264.0886.

Harraz, Hassan. (2013). Residual (eluvial or laterite) Mineral Deposits. 10.13140/RG.2.1.3788.3765.

Hashim, Mazlan. (2012). Identifying areas of high economic-potential copper mineralization using ASTER data in the Urumieh-Dokhtar Volcanic Belt, Iran. Advances in Space Research. 49. 753-769. 10.1016/j.asr.2011.11.028.

Hashim, Mazlan. (2012). The application of ASTER remote sensing data to porphyry copper and epithermal gold deposits. Ore Geology Reviews. 44. 1-9. 10.1016/j.oregeorev.2011.09.009.

Hedenquist, Jeffrey & Arribas, Antonio & Gonzalez-Urien, Eliseo. (2000). Exploration for Epithermal Gold Deposits. Reviews in Economic Geology. 13. 245-277.

Hermann, Joerg. (2022). Cycles of serpentines. Nature Geoscience. 15. 10.1038/s41561-022-01063-5.

Hermina, Maurice, Klitzsch, Eberhard, and K.List, Franz (1989): Stratigraphic Lexicon and Explantory Notes to the Geological Map of Egypt 1: 500.000. Conoco Inc. Berlin.

Hewson, Robert & Cudahy, Thomas & Drake-Brockman, Joseph & Meyers, Jayson & Hashemi, A.. (2006). Mapping geology associated with manganese mineralisation using spectral sensing techniques at Woodie Woodie, East Pilbara. Exploration Geophysics - EXPLOR GEOPHYS. 37. 10.1071/EG06389.

Hewson, Robert & Robson, D. & Mauger, Alan & Cudahy, Thomas & Thomas, Matilda & Jones, Simon. (2015). Using the Geoscience Australia-CSIRO ASTER maps and airborne geophysics to explore Australian geoscience. Spatial Science. 60. 10.1080/14498596.2015.979891.

Hosseinjanizadeh, Mahdieh & Tangestani, Majid & Velasco Roldán, Francisco & Yusta, I. (2014). Spectral characteristics of minerals in alteration zones associated with porphyry copper deposits in the middle part of Kerman copper belt, SE Iran. Ore Geology Reviews. 62. 191–198. 10.1016/j.oregeorev.2014.03.013.

Jain, Ronak & Bhu, Harsh & Purohit, Ritesh. (2020). Application of Thermal Remote Sensing Technique for Mapping of Ultramafic, Carbonate and Siliceous Rocks using ASTER Data in Southern Rajasthan, India. Current Science. 119. 954. 10.18520/cs/v119/i6/954-961.

John Pp. Rafferty (2012). minerals (Geology: landforms, minerals, and rocks). Britannica Educational Publishing. Ind Edition.

Kaliknowsski, Alkes & Oliver, Simon (2008). ASTER Mineral Exploration. ASL Mineral Exploration.

Korbel, P., & Novák, M. (2002). The Complete Encyclopedia of Minerals.

Kumari, Neeraj & Mohan, Chandra. (2021). Basics of Clay Minerals and Their Characteristic Properties. 10.5772/intechopen.97672.

Madani, A. & Emam, Ashraf. (2011). SWIR ASTER band ratios for lithological mapping and mineral exploration: A case study from El Hudi area, southeastern desert, Egypt. Arabian Journal of Geosciences. 4. 45-52. 10.1007/s12517-009-0059-8.

Maitre, R. & Streckeisen, A. & Zanettin, B. & Le Bas, M. & Bonin, Bernard & Bateman, P.. (2004). Igneous Rocks: A Classification and Glossary of Terms. Igneous Rocks: A Classification and Glossary of Terms, Edited by R. W. Le Maitre and A. Streckeisen and B. Zanettin and M. J. Le Bas and B. Bonin and P. Bateman, pp. 252. ISBN 0521619483. Cambridge, UK: Cambridge University Press, January 2005. 1.

Malainine, Cheikh Elwali & Raji, Otmane & Ouabid, M. & Khouakhi, Abdou & Bodinier, Jean-Louis & Laamrani, Ahmed & Messbahi, Hicham & Youbi, Nasrrddine & Boumehdi, Moulay Ahmed. (2021). An integrated ASTER-based approach for mapping carbonatite and iron oxide-apatite deposits.

Malekzadeh Shafaroudi, Azadeh & Karimpour, Mohammad Hassan. (2013). Hydrothermal Alteration Mapping in Northern Khur, Iran, Using ASTER Image Processing: a New Insight to the Type of Copper Mineralization. Acta Geologica Sinica. 87. 10.1111/1755-6724.12092.

Mars, John & Rowan, Lawrence. (2006). Regional mapping of phyllic- and argillic-altered rocks in the Zagros magmatic arc, Iran, using Advanced Spaceborne Thermal Emission and Reflection Radiometer (ASTER) data and logical operator algorithms. Geosphere. 2. 10.1130/GES00044.1.

Masoud, Alaa & Koike, Katsuaki. (2011). Morphotectonics inferred from the analysis of topographic lineaments auto-detected from DEMs: Application and validation for the Sinai Peninsula, Egypt. Tectonophysics. 510. 291-308. 10.1016/j.tecto.2011.07.010.

Mirsepahvand, Farzaneh & Jafari, Mohammadreza & Afzal, Peyman & Arian, Mohammad. (2022). Journal of Mining and Environment (JME) Identification of Alteration Zones using ASTER Data for Metallic Mineralization in Ahar region, NW Iran. 13. 309-324. 10.22044/jme.2022.11477.2135.

Misra, Kula. (2000). Precambrian Iron-Formations. 10.1007/978-94-011-3925-0_15.

Mohamed, Lamees. (2013). Dikes and Shear Zones Effects on Groundwater Flow in Southern Sinai, Egypt: Geophysical and Remote Sensing Constraints.

Moore, Farid & Rastmanesh, Fatemeh & Asadi, Hooshang & Modabberi, Soroush. (2008). Mapping mineralogical alteration using principal-component analysis and matched filter processing in the Takab area, north-west Iran, from ASTER data. International Journal of Remote Sensing. 29. 2851-2867. 10.1080/01431160701418989.

Moradpour, Hooman & Rostami Paydar, Ghodratolah & Feizizadeh, Bakhtiar & Blaschke, Thomas & Valizadeh Kamran, Khalil & M Muslim, Aidy & Hossain, Mohammad. (2021). Fusion of ASTER satellite imagery, geochemical and geology data for gold prospecting in the Astaneh granite intrusive, West Central Iran. International Journal of Image and Data Fusion. 10.1080/19479832.2021.1915395.

Mossa, Joann & James, Allan. (2013). Impacts of Mining on Geomorphic Systems. 10.1016/B978-0-12-374739-6.00344-4.

Mossa, Joann & James, Allan. (2021). Geomorphic Perspectives on Mining Landscapes, Hazards, and Sustainability. 10.1016/B978-0-12-818234-5.00159-0.

N.Lyberis (1988) :Tectonic evolution of the Gulf of Suez and Gulf of Aqaba . Journal of Tectonophysics . 153 . 1. 10.1016/0040-1951(88)90016-9

Ninomiya, Yoshiki. (2002). Mapping quartz, carbonate minerals, and mafic-ultramafic rocks using remotely sensed multispectral thermal infrared ASTER data. Proceedings of SPIE - The International Society for Optical Engineering. 191-202. 10.1117/12.459566.

Ninomiya, Yoshiki. (2004). Lithologic mapping with multispectral ASTER TIR and SWIR data. Proc. SPIE. 5234. 10.1117/12.511902.

Oha, Ifeanyi & Nnebedum, Okechukwu & Okonkwo, Ikenna. (2021). Alteration Mapping for Lead-Zinc-Barium Mineralization in Parts of the Southern Benue Trough, Nigeria, Using ASTER Multispectral Data. Earth Science Research. 10. 10.5539/esr.v10n1p61.

Parry, W. & Jasumback, M & Wilson, P.. (2002). Clay Mineralogy of Phyllic and Intermediate Argillic Alteration at Bingham, Utah. Economic Geology. 97. 221-239. 10.2113/gsecongeo.97.2.221.

Parsons, A.J., Abrahams, A.D. (2009). Geomorphology of Desert Environments. In: Parsons, A.J., Abrahams, A.D. (eds) Geomorphology of Desert

Environments. Springer, Dordrecht. https://doi.org/10.1007/978-1-4020-5719-9_1.

Pazand, Kamran & Pazand, Kaveh. (2020). Identification of hydrothermal alteration minerals for exploring porphyry copper deposit using ASTER data: a case study of Varzaghan area, NW Iran. Geology, Ecology, and Landscapes. 6. 1-7. 10.1080/24749508.2020.1813371.

Pirajno, F. (1992). Hydrothermal Alteration. In: Hydrothermal Mineral Deposits. Springer, Berlin, Heidelberg. https://doi.org/10.1007/978-3-642-75671-9_5

Rajendran, Sankaran & Nasir, Sobhi. (2013). Rajendran S, Nasir S. (2013). Mapping of manganese potential areas using ASTER satellite data in parts of Sultanate of Oman. International Journal of Geosciences and Geomatics. 1/2, 92-101. International Journal of Geosciences and Geomatics. 92-101.

Rajendran, Sankaran & Nasir, Sobhi. (2014). Hydrothermal altered serpentinized zone and a study of Ni-magnesioferrite-magnetite-awaruite occurrences in Wadi Hibi, Northern Oman Mountain: Discrimination through ASTER mapping. Ore Geology Reviews. 62. 10.1016/j.oregeorev.2014.03.016.

Rajendran, Sankaran & Nasir, Sobhi. (2017). Characterization of ASTER spectral bands for mapping of alteration zones of Volcanogenic Massive Sulphide (VMS) deposits. Ore Geology Reviews.

Rasouli Beirami, Meisam & Tangestani, Majid. (2020). A New Band Ratio Approach for Discriminating Calcite and Dolomite by ASTER Imagery in Arid and Semiarid Regions. Natural Resources Research. 29. 10.1007/s11053-020-09648-w.

Salehi, Sara & Olsen, Símun & Pedersen, Christian & Thorning, Leif. (2019). ASTER data analysis applied to mineral and geological mapping in North East Greenland Documentation of the NEG ASTER Project. 10.13140/RG.2.2.15404.00642.

Salem, S. & El-Sharkawi, Mohamed & Alfy, Z. & Ahmed, Syed. (2018). The use of ASTER data and geochemical analyses for the exploration of gold at Samut area, South Eastern Desert of Egypt. Arabian Journal of Geosciences. 11. 10.1007/s12517-018-3793-y.

Scheller, Eva & Swindle, Carl & Grotzinger, John & Barnhart, Holly & Bhattacharjee, Surjyendu & Ehlmann, Bethany & Farley, Ken & Fischer, Woodward & Greenberger, Rebecca & Ingalls, Miquela & Martin, Peter & Osorio-Rodriguez, Daniela & Smith, Ben. (2021). Formation of

Magnesium Carbonates on Earth and Implications for Mars. Journal of Geophysical Research: Planets. 126. 10.1029/2021JE006828.

Sengupta, Arnab & Das Adhikari, Manik & Maiti, Sabyasachi & Maiti, Soumya & Mahanta, Pankajini & Bhaumick, Siddhartha. (2018). Identification and mapping of high-potential iron ore alteration zone across Joda, Odisha using ASTER and EO-1 hyperion data. Journal of Spatial Science. 64. 1-24. 10.1080/14498596.2018.1485120.

Shendi, El-Arabi & Ismail, A. & Attia, Tamer. (2008). On the use of gravity and magnetic anomalies for locating probable areas of metallic mineralization in South Sinai, Egypt. Arabian Journal of Geosciences. 1. 137-147. 10.1007/s12517-008-0013-1.

Singhal, Bhvvya & Gupta, R.. (2010). Applied Hydrogeology of Fractured Rocks. 10.1007/978-94-015-9208-6.

Thompson, A.J., Thompson, J.F., & Dunne, K.P. (1996). Atlas of alteration: a field and petrographic guide to hydrothermal alteration minerals.

Thompson, J. F. H., Thompson, A. J. B., Allen, R. L., Geological Association of Canada., & University of British Columbia. (1996). Atlas of alteration: A field and petrographic guide to hydrothermal alteration minerals. St. John's, Nfld: Geological Association of Canada, Mineral Deposits Division.

Yaxley, Gregory & Anenburg, Michael & Tappe, Sebastian & Decrée, Sophie & Guzmics, Tibor. (2022). Carbonatites: Classification, Sources, Evolution, and Emplacement. Annual Review of Earth and Planetary Sciences. 50. 261-293. 10.1146/annurev-earth-032320-104243.

Yousefi, S.J., Ranjbar, H., Alirezaei, S., Dargahi, S (2018). Discrimination of Sericite Phyllic and Quartz-Rich Phyllic Alterations by Using a Combination of ASTER TIR and SWIR Data to Explore Porphyry Cu Deposits Hosted by Granitoids, Kerman Copper Belt, Iran. J Indian Soc Remote Sens 46, 717–727. https://doi.org/10.1007/s12524-017-0745-z